

Ab Initio Study of the Ferroelectric Transition in Cubic Pb_3GeTe_4

Eric Cockayne and Karin M. Rabe

Department of Applied Physics, Yale University, P.O. Box 208284, New Haven, CT 06520-8284

(January 7, 2022)

Abstract

In the substitutionally disordered narrow-gap semiconductor $\text{Pb}_{1-x}\text{Ge}_x\text{Te}$, a finite-temperature cubic-rhombohedral transition appears above a critical concentration $x \approx 0.005$. As a first step towards a first-principles investigation of this transition in the disordered system, a (hypothetical) ordered cubic Pb_3GeTe_4 supercell is studied. First principles density-functional calculations of total energies and linear response functions are performed using the conjugate-gradients method with ab initio pseudopotentials and a plane-wave basis set. Unstable modes in Pb_3GeTe_4 are found, dominated by off-centering of the Ge ions coupled with displacements of their neighboring Te ions. A model Hamiltonian for this system is constructed using the lattice Wannier function formalism. The parameters for this Hamiltonian are determined from first principles. The equilibrium thermodynamics of the model system is studied via Metropolis Monte Carlo simulations. The calculated transition temperature, T_c , is approximately 620K for the cubic Pb_3GeTe_4 model, compared to the experimental value of $T_c \approx 350\text{K}$ for disordered $\text{Pb}_{0.75}\text{Ge}_{0.25}\text{Te}$. Generalization of this analysis to the disordered $\text{Pb}_{1-x}\text{Ge}_x\text{Te}$ system is discussed.

Typeset using REVTeX

I. INTRODUCTION

Numerous substitutionally disordered ferroelectrics exhibit structural phase transitions in which the nature of the phase transition changes as a function of composition. Examples include $\text{Ba}_{1-x}\text{Sr}_x\text{TiO}_3$ ¹, $\text{PbZr}_{1-x}\text{Ti}_x\text{O}_3$ ^{2,3}, and $\text{Pb}_{1-x}\text{Ge}_x\text{Te}$ ⁴. $\text{Pb}_{1-x}\text{Ge}_x\text{Te}$ is an ideal system for the development of first-principles methods to investigate the effect of substitution on structural phase transitions for several reasons. First, the unit cells of the endpoint compounds are small. Pure PbTe and GeTe have only two atoms and ten valence electrons per unit cell, as opposed to five atoms and 24 or more valence electrons per unit cell in the perovskite oxide ferroelectrics. Secondly, the phase diagram in $\text{Pb}_{1-x}\text{Ge}_x\text{Te}$ is rather simple.⁴ Pure PbTe has a rocksalt structure that is stable to zero temperature. Pure GeTe also has the rocksalt structure at high temperature but undergoes a structural phase transition, indicated in Figure 1, to a rhombohedral phase at a critical temperature $T_c \approx 670\text{K}$.⁵ As the Ge concentration x decreases from 1 to 0, T_c for a cubic-rhombohedral phase transition decreases smoothly to zero at $x \approx 0.005$.^{4,6} Finally, there are existing phenomenological and empirical models for this transition.⁷⁻¹⁰ These models focus on the role of Ge off-centering^{7,8} in the phase transition. Off-centering is observed in a number of compounds where there is a mismatch between the ionic radii of two species that statistically occupy the same kind of site.¹¹ There is direct experimental evidence for off-centering in $\text{Pb}_{1-x}\text{Ge}_x\text{Te}$. The extended X-ray-absorption fine-structure measurements of Islam and Bunker¹⁰ show two peaks in the distribution function for Ge-Te distances both above and below T_c , as opposed to the single peak that would be seen if the Ge atoms were located at the centers of the octahedra formed by their first-neighbor Te atoms. The phenomenological and empirical models previously considered provide a reference for comparison with the model derived from first principles here.

Model Hamiltonians based on ab-initio calculations have been successfully constructed for a number of stoichiometric ferroelectrics and related materials, including GeTe ¹², PbTiO_3 ¹³, PbZrO_3 ¹⁴, BaTiO_3 ^{15,16}, SrTiO_3 ¹⁷ and KNbO_3 ¹⁸. In constructing these models, the high-

symmetry average structure of the high-temperature phase is chosen as a reference structure. Normal mode dispersion relations and eigenfunctions are calculated to determine the unstable modes. The normal mode branches containing the unstable modes form a basis for the ionic displacement subspace determining, by projection, an effective Hamiltonian. Via a linear transformation, a localized lattice Wannier function¹⁹ (LWF) basis is found. The energy is expanded in powers of the lattice Wannier function coordinates and strain and the coefficients in the expansion are determined from a set of ab-initio calculations.

In a substitutionally disordered system, it is not enough to include only the lattice degrees of freedom. Configurational entropy also plays an important role; the partition function, from which all thermodynamic properties can be obtained, includes a sum over all possible configurations. Different *fixed* configurations will undergo structural phase transitions at different temperatures. Furthermore, the nature of the configurations whose properties dominate in the thermodynamic limit will itself depend on temperature. However, it is not necessary to investigate all possible configurations in order to model a phase transition in a disordered system. In fact, if a model can be formulated in terms of intersite interactions that decay rapidly with distance to some asymptotic form, only a small number of configurations need to be explicitly calculated from first principles.

In this work, we investigate a single $\text{Pb}_{1-x}\text{Ge}_x\text{Te}$ configuration: the *ordered* 8 atom Pb_3GeTe_4 cubic cell ($x = 0.25$), shown in Figure 2. This configuration was chosen for several reasons: (1) it is toward the Pb-rich end of the phase diagram, which is appropriate for studying how adding a small concentration of Ge to PbTe “turns on” a phase transition at zero temperature, (2) it contains the minimum number of atoms per cell (eight) for any $x \leq 0.25$ and (3) among the eight atom cells with $x = 0.25$, it has the highest point symmetry. The small size and high symmetry of the unit cell for cubic Pb_3GeTe_4 makes *ab initio* calculations relatively computationally inexpensive. Our calculation of T_c for this system provides a benchmark for comparison with T_c for other configurations and for the ensemble average at the same composition.

This paper is organized as follows. Section II describes the general principles governing

the construction of model Hamiltonians and the lattice Wannier function method for determining the effective Hamiltonian subspace. In Section III, these methods are applied to the specific case of cubic Pb_3GeTe_4 and a model Hamiltonian is obtained. The model Hamiltonian is used in a classical Monte Carlo simulation in Section IV to obtain the transition temperature and order of the cubic- rhombohedral phase transition in this system. The results are further discussed in Section V, including their implications for the substitutionally disordered $\text{Pb}_{1-x}\text{Ge}_x\text{Te}$ system. Conclusions are given in Section VI.

II. CONSTRUCTION OF MODEL HAMILTONIANS

At the level of the Born-Oppenheimer approximation for electronic energy, the classical partition function Z for a disordered system on a fixed lattice is

$$Z = \sum_{\{\sigma_j\}} \int d\{\mathbf{u}_j\} \int d\{\dot{\mathbf{u}}_j\} \int d\mathbf{e} \exp[(-\beta E(\{\sigma_j\}, \{\mathbf{u}_j\}, \{\dot{\mathbf{u}}_j\}, \mathbf{e})], \quad (2.1)$$

where $\{\sigma_j\}$ represents the chemical configuration, *i.e.* which type of ion occupies each site j , \mathbf{e} is the homogeneous strain tensor, $\{\mathbf{u}_j\}$ is the set of ionic displacements defined with respect to some reference structure for the given chemical configuration and strain, and $\{\dot{\mathbf{u}}_j\}$ is the set of ionic velocities. If, in addition, the ionic motion is treated classically, the integral over $\{\dot{\mathbf{u}}_j\}$ leads to a trivial \mathbf{u} -independent factor, and the partition function can be rewritten as

$$Z \propto \sum_{\{\sigma_j\}} \int d\{\mathbf{u}_j\} \int d\mathbf{e} \exp[(-\beta E(\{\sigma_j\}, \{\mathbf{u}_j\}, \mathbf{e})], \quad (2.2)$$

The partition function 2.2 can be rewritten $Z \propto \sum_{\{\sigma_j\}} Z(\{\sigma_j\})$, where $Z(\{\sigma_j\})$ is the partition function for the ensemble corresponding to the single chemical configuration $\{\sigma_j\}$. In what follows, we consider only one chemical configuration, so the configuration label σ_j will be dropped. The partition function now simplifies to

$$Z \sim \int d\{\mathbf{u}_j\} \int d\mathbf{e} \exp[(-\beta E(\{\mathbf{u}_j\}, \mathbf{e})]. \quad (2.3)$$

In general, $E(\{\mathbf{u}_j\}, \mathbf{e})$ can be expanded as a Taylor series in powers of \mathbf{u}_j and \mathbf{e} . If the reference structure is at an energy extremum, then the linear terms in the expansion vanish:

$$E(\{\mathbf{u}_i\}, \mathbf{e}) = E^{(0)} + E^{(2)}(\{\mathbf{u}_j\}, \mathbf{e}) + E^{(3)}(\{\mathbf{u}_j\}, \mathbf{e}) + \dots \quad (2.4)$$

The harmonic term, $E^{(2)}(\{\mathbf{u}_j\}, \mathbf{e})$ is the sum of a lattice term

$$\sum_{ij\alpha\beta} F_{ij\alpha\beta} u_{i\alpha} u_{j\beta}, \quad (2.5)$$

where F is the force constant matrix, a strain term

$$\sum_{\alpha\beta\gamma\delta} c_{\alpha\beta\gamma\delta} e_{\alpha\beta} e_{\gamma\delta}, \quad (2.6)$$

where c is the elastic constant tensor, and a strain-coupling term

$$\sum_{i\alpha\beta\gamma} g_{i\alpha\beta\gamma} u_{i\alpha} e_{\beta\gamma}, \quad (2.7)$$

where g is the strain-coupling tensor. By the usual change of variable to normal mode variable, $\{\mathbf{u}_j\} = \sum_{\nu} a_{\nu} \epsilon_{\nu}$, the harmonic lattice term is reduced to a single sum:

$$\sum_{ij\alpha\beta} F_{ij\alpha\beta} u_{i\alpha} u_{j\beta} = \frac{1}{2} \sum_{\nu} m_{\nu} \omega_{\nu}^2 a_{\nu}^2, \quad (2.8)$$

where a_{ν} is the amplitude, ϵ_{ν} the (normalized) ionic displacement pattern, ω_{ν} the frequency, and m_{ν} the mode effective mass for normal mode ν .

In what follows, it is assumed that the fixed configuration is periodic. Then the normal mode label ν can be replaced by $\mathbf{k}i\alpha$, where \mathbf{k} is the wavevector, i the symmetry-invariant subspace and α the branch of the normal mode dispersion curves on which the mode lies. For example, in a structure with two atoms per unit cell, $i = 1$ represents the acoustic modes, $i = 2$ the optical modes, and in each subspace $\alpha = 1$ labels the longitudinal and $\alpha = 2, 3$ labels the two transverse branches.

If the extremum or reference structure is a saddle point in the energy surface rather than a minimum, some of the normal modes will be unstable ($\omega_{\mathbf{k}i\alpha}^2 < 0$). As described in detail by Rabe and Waghmare^{20,19}, the model Hamiltonian approach to structural phase transitions

associated with soft phonons aims to reduce the ionic degrees of freedom to those of the “effective Hamiltonian” subspace that contains the important anharmonic terms in Eq. 2.4. All normal mode subspaces i that contain unstable modes must be included in the effective Hamiltonian subspace. An expansion of the total energy in these degrees in freedom requires higher-order terms in order to stabilize the structure at a finite distortion. As the simplest approximation, terms are kept to only harmonic order in the subspace complementary to the effective Hamiltonian subspace and higher order mixing of the effective Hamiltonian subspace with the complementary subspace is neglected. This approximation is valid to the extent that the magnitude of the neglected higher order terms is small for all ionic displacement patterns that contribute significantly to Z , *i.e.* those where $E(\{\mathbf{u}_j\}, \mathbf{e})$ is small. Integration over the complementary subspace gives a structure-independent contribution to Z which can be neglected. The remaining terms in E give an effective Hamiltonian \mathcal{H}_{eff} . Integration of \mathcal{H}_{eff} over the effective Hamiltonian subspace is sufficient to reproduce the dependence of the structure on temperature.

A change in variables allows the basis of the effective Hamiltonian subspace to be converted into one where the displacements are localized, *i.e.* a lattice Wannier function (LWF) basis $\mathbf{w}_\mathbf{R}$ ¹⁹. This procedure is analogous to that which des Cloizeaux²¹ gave for determining *electronic* Wannier functions for a multidimensional subspace; except that the periodic functions are now ionic displacement patterns.¹⁹ For simplicity, we assume that the effective Hamiltonian subspace consists of only a single normal mode subspace $i = 1$, drop the subscript i , and let $\epsilon_{\mathbf{k}\alpha}$ label the normal modes in this subspace. The LWF is given in terms of the normal modes by

$$w_{\beta\mathbf{R}} = \frac{V}{(2\pi)^3} \int_{BZ} d\mathbf{k} \left(\sum_{\alpha} C_{\alpha\beta}(\mathbf{k}) \epsilon_{\mathbf{k}\alpha} e^{i(\phi_{\mathbf{k}\alpha} - \mathbf{k} \cdot \mathbf{R})} \right). \quad (2.9)$$

The subscript β labels the components of the LWF. The number of components of $\mathbf{w}_\mathbf{R}$ is equal to the number of branches in the effective Hamiltonian normal mode subspace. The matrix $C(\mathbf{k})$ is included so that the polarizations of the different normal mode branches are correctly related to the LWF components across the Brillouin zone. The phases $\phi_{\mathbf{k}\alpha}$ are

very important. They are chosen to make the ionic displacement pattern corresponding to \mathbf{w} both as local as possible and with as high a symmetry as possible. By construction, the LWF has translational symmetry: $T_{\mathbf{R}'}(w_{\beta\mathbf{R}}) = w_{\beta\mathbf{R}+\mathbf{R}'}$, where \mathbf{R}' is any lattice vector.

The normal modes are given in terms of the LWF basis via the inverse transform

$$[e^{i\phi_{\mathbf{k}\alpha}}]\epsilon_{\mathbf{k}\alpha} = \sum_{\mathbf{R}\beta} (C^{-1})_{\alpha\beta} w_{\beta\mathbf{R}} e^{i\mathbf{k}\cdot\mathbf{R}}. \quad (2.10)$$

Any displacement pattern \mathbf{u}_j in the effective Hamiltonian subspace can be written as

$$\mathbf{u}_j = \sum_{\mathbf{k}\alpha} a_{\mathbf{k}\alpha} \epsilon_{\mathbf{k}\alpha}. \quad (2.11)$$

Using Eq. 2.10, and changing the order of the summation, we obtain

$$\mathbf{u}_j = \sum_{\mathbf{R}\beta} w_{\beta\mathbf{R}} \left[\sum_{\mathbf{k}\alpha} (C^{-1})_{\alpha\beta} a_{\mathbf{k}\alpha} e^{i(\mathbf{k}\cdot\mathbf{R} - \phi_{\mathbf{k}\alpha})} \right] = \sum_{\mathbf{R}\beta} w_{\beta\mathbf{R}} \xi_{\beta\mathbf{R}}. \quad (2.12)$$

The new vector parameter $\vec{\xi}_{\mathbf{R}}$ gives the displacement field via Eq. 2.12 and provides the basis for a spin-like model of the system.

III. MODEL HAMILTONIAN CONSTRUCTION FOR Pb_3GeTe_4

In this section, we describe the construction of the effective Hamiltonian subspace and the explicit expression for the model Hamiltonian for Pb_3GeTe_4 from first-principles density-functional calculations within the local-density approximation (LDA). Bachelet, Hammann and Schlüter pseudopotentials²² were used for each species in the two-projector Kleinman-Bylander form.^{23,24} For Pb and Te, the d potential was taken as local; for Ge, a d local potential was found to give spurious low-energy “ghost” states^{25,26} and so a p local potential was chosen. Total energy calculations were done using the CASTEP 2.1 program of Payne *et al.*²⁷ CASTEP 2.1 performs conjugate gradients minimization²⁸ of the LDA density functional total energy in the Kohn-Sham formalism.²⁹ The exchange-correlation energy was Perdew and Zunger’s parameterization³⁰ of the Ceperley-Alder values³¹ for the uniform electron gas. The calculations were performed for a 8-atom unit cell with a 300 eV cutoff for the

plane wave basis set (about 3000 plane waves per k-point), a 4 by 4 by 4 Monkhorst-Pack³² k-point set, and a 36 by 36 by 36 real-space grid for the charge density. Force constant matrices at the high-symmetry $\mathbf{q} \neq 0$ points in the Brillouin zone and Born effective charges were computed using density-functional perturbation theory^{33,34} in the variational formulation.³⁵ At $\mathbf{q} = 0$, the force constant matrix was computed using Hellmann-Feynman forces, as described in more detail below. Pulay corrections³⁶ were added to the total energy results as described in the Appendix.

We began with Pb_3GeTe_4 in a high-symmetry reference structure. The structure, shown in Figure 2, is produced by replacing a cubic superlattice of Pb ions in the PbTe rocksalt structure with Ge ions. There are eight atoms per unit cell. The structure has full cubic symmetry (space group $\text{Pm}\bar{3}\text{m}$). The Ge occupies the cell corner (Wyckoff position 1(a)) and the three Pb's occupy the face centers (3(c)). The four Te's occupy two crystallographically distinct positions: the edge centers (3(d)) and the cube center (1(b)). Although this structure is not the minimum-energy structure, the forces on all ions are zero by symmetry, and the problem of relaxation can thus be neglected (note this is not true for the general case of partial $\text{Pb} \rightarrow \text{Ge}$ substitution). Furthermore, the Pb_3GeTe_4 structure with the lattice constant a which minimizes the total energy is at an extremum of the $E(\{\mathbf{u}_i\}, \mathbf{e})$ energy surface, so that it can be used as a reference structure in the analysis of Section II. We found $a = 6.275 \text{ \AA}$ for cubic Pb_3GeTe_4 . Although there is no experimental cubic Pb_3GeTe_4 sample with which this result can be prepared, we can estimate the “experimental” lattice parameter in two different ways as follows. First, we extrapolate the experimental lattice parameters for PbTe at room temperature³⁷ and for GeTe at the cubic-rhombohedral phase transition temperature³⁸ to zero temperature via the thermal expansion coefficient of PbTe at room temperature³⁷ and then average the results assuming Vegard’s law to obtain $a = 6.307(2) \text{ \AA}$. Second, we estimate the experimental lattice parameter for disordered $\text{Pb}_{0.75}\text{Ge}_{0.25}\text{Te}$ at room temperature and the thermal expansion coefficient for nearby compositions via the figures in Reference 4 and then extrapolate to zero temperature to obtain $a = 6.311(1) \text{ \AA}$. The two estimates are in good agreement. The LDA lattice parameter is about 0.5% lower

than the “experimental” value. This magnitude of lattice constant underestimate is typical of LDA calculations.³⁹

Next, we identified the lattice instabilities of the reference structure. The force constants at $\mathbf{q} = 0$ were found by displacing each ion in turn and then calculating the Hellmann-Feynman forces. Anharmonic effects were found to be significant in Pb_3GeTe_4 and thus it was necessary to calculate the forces for small (0.001 to 0.01 Å) displacements and extrapolate the force constant values to zero displacement in order to obtain high precision. For comparison, we also calculated the force constant matrix at $\mathbf{q} = 0$ using the density-functional perturbation theory method. The latter results, however, violated the acoustic sum rule by as much as $0.1 \text{ eV}/\text{\AA}^2$, whereas the maximum violation of the acoustic sum rule for the extrapolated Hellmann-Feynman forces was only $10^{-4} \text{ eV}/\text{\AA}^2$. The discrepancy between the force constant matrix elements found by the two methods was largest for the diagonal terms. In order to avoid significant acoustic sum rule violation corrections, at $\mathbf{q} = 0$ we used the extrapolated Hellmann-Feynman forces.

Diagonalization of the resulting $\mathbf{q} = 0$ dynamical matrix yielded a single unstable mode at Γ (see Table I), with symmetry Γ_{15} . The fact that it is strongly dominated by Ge motion led us to choose a single LWF centered on Ge with Γ_{15} (vector) symmetry. To construct the effective Hamiltonian subspace, it is therefore necessary only to investigate those $\mathbf{q} \neq 0$ normal modes compatible with this choice of LWF symmetry. We performed $\mathbf{q} \neq 0$ linear-response calculations to calculate the normal mode frequencies and eigenvectors for all such modes at the BZ points Γ , R , X and M (Table I). For each label⁴⁰ X'_1 , X'_5 , M'_1 , M'_5 and R_{15} , the lowest energy mode also has a large component of Ge motion (see Tables I and II), and is therefore easily identified as a mode belonging to the effective Hamiltonian subspace.

Substitution of the first-principles results for the ionic displacements of the selected normal modes into Eq. 2.10 leads to a set of linear equations, which can be solved to obtain the LWF. To obtain the exact LWF, which in general involves nonzero ionic displacements out to infinite distance, it would be necessary to include an infinite number of independent normal modes in the analysis. We expect, however, that the ionic displacements corresponding to

the lattice Wannier function decrease rapidly with distance, in analogy to the behavior of electronic Wannier functions²¹ and of the lattice Wannier function for PbTiO_3 .¹³ A good approximation to such a LWF can be obtained by setting all ionic displacements equal to zero outside of some finite region. The remaining finite set of ionic displacements can be determined from a finite set of normal modes via Eq. 2.9. For cubic Pb_3GeTe_4 , we used all the modes of Table II. All modes were normalized so that the sum of the squared ionic displacements was 1 \AA^2 per primitive cell. For these high symmetry points, the normal modes can be chosen so that Ge motion is always strictly along a Cartesian direction and thus the matrix C in Eq. 2.9 is the unit matrix. The phases $\phi_{\mathbf{k}\alpha}$ are already incorporated into Table II and are chosen so that Ge motion is always in the same direction. The included modes yielded a set of 21 independent linear equations and therefore allowed the 21 independent components of ionic displacement shown in Table III to be determined. The displacements corresponding to the approximate LWF involve all ions out to $(\sqrt{5}/2)a$ from the central Ge ion and some ions as far as $1.5a$ away.

As can be seen from Table III and Figure 3, the LWF satisfies the locality assumption very well, with first-near neighbor Te displacements only 0.27 times the central Ge displacement, second near-neighbor Pb displacements up to 0.14 times the Ge displacement and all further-neighbor displacements less than 0.05 times the central Ge displacement. Note that although the LWF component shown transforms as the z component of a vector, individual ionic displacements, such as the Pb displacements shown in Figure 3, can be in directions other than z . Henceforth, we use units in which a dimensionless local distortion amplitude of 1 in the z direction corresponds to the displacements shown in Table III.

To summarize, the structure-dependent part of the partition function for Pb_3GeTe_4 should depend only on a subspace of the full ionic displacement space, which can be used to generate an effective Hamiltonian. So far, we have found a good approximation to $\mathbf{w}_{\mathbf{R}}$, the lattice Wannier function basis for the effective Hamiltonian subspace, which includes the unstable normal modes. We have a spin-like representation in which there is a one-to-one correspondence between ionic displacement patterns in the effective Hamiltonian subspace

and the magnitudes and directions of a set of vectors located on each Ge ion. We will now describe the model Hamiltonian for Pb_3GeTe_4 , obtained by (1) expanding the effective Hamiltonian energy per unit cell $\mathcal{H}_{eff}(\{\vec{\xi}_i\}, \mathbf{e})/N$ in powers of $\vec{\xi}_i$ and strain \mathbf{e} , (2) truncating this expansion, and (3) determining the coefficient for each term from first-principles calculations.

Previous *ab initio* studies on perovskite ferroelectrics such as BaTiO_3 ¹⁵ and PbTiO_3 ¹³ have led to models of the same nature as that presented here, namely a set of interacting vector spins sitting on Wyckoff positions of full cubic symmetry for a cubic lattice with underlying space group $Pm3m$. For Pb_3GeTe_4 , we used the same truncations in the expansion of \mathcal{H}_{eff} as was used for the PbTiO_3 model.¹³ We verified that the terms retained were necessary and sufficient to accurately fit the corresponding *ab initio* results. Various contributions to the model Hamiltonian will now be considered in turn.

The total energy contains a structure-independent constant term

$$U_0/N \tag{3.1}$$

giving the energy of the high symmetry Pb_3GeTe_4 reference structure ($\vec{\xi}_i = \mathbf{e} = 0$). In the case of disordered systems, differences in reference structure energy are important for comparing different chemical configurations. The value of U_0/N for cubic Pb_3GeTe_4 is given in the Appendix. Since only one cation configuration is considered in this work, the value of U_0/N does not affect subsequent results.

The lowest order terms which depend on the local distortions $\{\vec{\xi}_i\}$ are harmonic, with a local contribution $U_{lh} = \sum_i A|\vec{\xi}_i|^2$ and an intersite pair contribution $U_{ph} = \sum_{i,j} a_{ij\alpha\beta} \xi_{i\alpha} \xi_{j\beta}$. At long range, we expect the intersite pair interaction to approach the dipole-dipole form, while at shorter range, there should be significant corrections due to higher order multipole effects, induced charge redistributions and direct overlap of the ionic displacement patterns. We thus split U_{ph} into the sum of a long-range dipole-dipole term, U_{dd} , and a short range “correction” term, U_{sr} .

The energy of a system of dipoles of moment $\vec{\mu}$ in a medium of electronic dielectric

constant ϵ_∞ is given by:⁴¹

$$U_{dd}(\{\vec{\mu}_i\})/N = \frac{1}{N} \sum_i \sum_{\vec{d}} \frac{1}{\epsilon_\infty} \frac{(\vec{\mu}_i \cdot \vec{\mu}_{i+\vec{d}} - 3(\vec{\mu}_i \cdot \hat{d})(\vec{\mu}_{i+\vec{d}} \cdot \hat{d}))}{|\vec{d}|^3}. \quad (3.2)$$

The sum over \vec{d} is a sum over all interdipole separations, $\vec{\mu}_i$ is the dipole moment at site i , and $\vec{\mu}_{i+\vec{d}}$ is the dipole moment of the dipole at distance \vec{d} from the dipole at site i .

To make use of Eq. 3.2, we need to know the dipole moments $\vec{\mu}_i$ corresponding to local distortions $\vec{\xi}_i$. Since the dipole moment at $\vec{\xi} = 0$ is zero via centrosymmetry, the dipole moment for nonzero $\vec{\xi}$ is simply the sum of the polarizations \vec{P}_j induced by individual ionic displacements \vec{u}_j specified by the given $\vec{\xi}_i$:

$$\vec{\mu} = \sum_j \vec{P}_j(\vec{u}_j(\vec{\xi}_i)). \quad (3.3)$$

For small displacements, the \vec{P}_j are determined by the Born effective charge tensor for the ion j , defined as the differential change in total polarization due to displacement of that ion:

$$Z_{j\alpha\beta}^* \equiv \frac{\partial P_\alpha}{\partial u_{j\beta}}. \quad (3.4)$$

Symmetry considerations reduce the number of independent terms in the Born effective charge tensors for Pb_3GeTe_4 . Though our Pb_3GeTe_4 structure has cubic symmetry, not all of the ions sit at centers of full cubic symmetry. The Ge and Te(1) ions sit at centers of cubic symmetry, while the Pb and Te(2) ions fill the two Wyckoff positions of multiplicity three, each of which is a center of tetragonal symmetry. The Born effective charge tensor is still diagonal under tetragonal symmetry, but the axial and perpendicular values are different. Thus, there are 6 independent Born effective charge tensor components in the Pb_3GeTe_4 cell, one each for Ge and Te(1) and two each for Pb and Te(2). The Born effective charge tensors, obtained from linear response calculations for cubic Pb_3GeTe_4 at the equilibrium LDA lattice constant, are shown in Table IV. The sum of the Born effective charges $\sum_j^{\text{unitcell}} (\frac{1}{3}Z_{j\parallel}^* + \frac{2}{3}Z_{j\perp}^*)$ as determined via linear response calculations was -0.36 . This violation of charge neutrality is a consequence of finite k-point sampling.⁴² We corrected for it⁴² by adding the same constant 0.045 to all diagonal Born effective charge tensor components. The diagonal cation

(Te) effective charge components are in the range +6 to +8 (−6 to −8). These effective charges are anomalously large compared to the formal valence charge states, but consistent in magnitude with those found experimentally⁴³ and theoretically⁴⁴ for binary group IV tellurides.

Since the u_j are proportional to $\vec{\xi}_i$ (Eq. 2.12), the dipole moment $\vec{\mu}$ can be written simply as

$$\vec{\mu}_i = \sum_j \mathbf{Z}_j^* \mathbf{u}_j(\vec{\xi}_i) = \overline{Z}^*(\vec{\xi}_i), \quad (3.5)$$

where symmetry leads to a scalar mode effective charge parameter \overline{Z}^* , which for Pb_3GeTe_4 has the value 12.10 eÅ. Eq. 3.2 can then be written in terms of $\vec{\xi}$ as follows:

$$U_{dd}(\{\vec{\xi}_i\})/N = \frac{1}{N} \sum_i \sum_{\vec{d}} \frac{(\overline{Z}^*)^2}{\epsilon_\infty} \frac{(\vec{\xi}_i \cdot \vec{\xi}_{i+\vec{d}} - 3(\vec{\xi}_i \cdot \hat{d})(\vec{\xi}_{i+\vec{d}} \cdot \hat{d}))}{|\vec{d}|^3} \quad (3.6)$$

The other material specific parameter needed in Eq. 3.2 is ϵ_∞ . By symmetry, the dielectric tensor is isotropic in cubic Pb_3GeTe_4 . Via linear response methods, we calculated $\epsilon_\infty = 46.7$. The experimental value for PbTe is 33-34 at room temperature^{43,45} and 40 at zero temperature.⁴⁵ For GeTe , the measured value⁴³ at room temperature is 36. For $\text{Pb}_{1-x}\text{Ge}_x\text{Te}$, ϵ_∞ measurements are available for $x = 0.07$, for which the values obtained are about 39 at room temperature, 41 for the cubic phase just above the phase transition and 40 at zero temperature.⁴⁵ Our value for ϵ_∞ is somewhat higher than the value obtained from interpolation of the experimental values, consistent with the general tendency of LDA to overestimate dielectric constants.⁴⁶

Next, consider U_{sr} , the short-range correction term in the intersite pair interaction. The force constant matrix elements determined in a series of $\mathbf{q} \neq 0$ linear response calculations, along with the corresponding ionic displacement fields, allow the total harmonic energy $U_{lh} + U_{ph}$ to be determined. These are given in Table V for the various high-symmetry \mathbf{q} points used in determining the LWF. For each normal mode used to construct the LWF, we calculated the dipole-dipole interaction energy U_{dd} via Eq. 3.6. We then subtracted the dipole part from the total harmonic energy to obtain $U_{sr}(\{\vec{\xi}_i\})$.

As in the case of the LWF itself, the information obtained from a finite set of independent q points limits the number of interaction coefficients that can be determined. We include here all symmetry-adapted couplings to third neighbors in the cubic lattice (or sixth neighbor cations). There are two independent coefficients at first neighbor

$$U_{sr}(\{\vec{\xi}_i\})/N = \frac{1}{N} \sum_i \sum_{\hat{d}=nn1} [b_L(\vec{\xi}_i \cdot \hat{d})(\vec{\xi}_{i+\hat{d}} \cdot \hat{d}) + b_T(\vec{\xi}_i \cdot \vec{\xi}_{i+\hat{d}} - (\vec{\xi}_i \cdot \hat{d})(\vec{\xi}_{i+\hat{d}} \cdot \hat{d}))], \quad (3.7)$$

three at second neighbor

$$\begin{aligned} & + \frac{1}{N} \sum_i \sum_{\hat{d}=nn2} [d_L(\vec{\xi}_i \cdot \hat{d})(\vec{\xi}_{i+\hat{d}} \cdot \hat{d}) + d_{T1}(\vec{\xi}_i \cdot \hat{d}_1)(\vec{\xi}_{i+\hat{d}} \cdot \hat{d}_1) \\ & + d_{T2}(\vec{\xi}_i \cdot \hat{d}_2)(\vec{\xi}_{i+\hat{d}} \cdot \hat{d}_2)], \end{aligned} \quad (3.8)$$

and two at third neighbor

$$+ \frac{1}{N} \sum_i \sum_{\hat{d}=nn3} [f_L(\vec{\xi}_i \cdot \hat{d})(\vec{\xi}_{i+\hat{d}} \cdot \hat{d}) + f_T(\vec{\xi}_i \cdot \vec{\xi}_{i+\hat{d}} - (\vec{\xi}_i \cdot \hat{d})(\vec{\xi}_{i+\hat{d}} \cdot \hat{d}))]. \quad (3.9)$$

In these expressions, \hat{d} is a unit vector that is summed over all directions from a site i to the neighbors in a given shell. For second neighbors, a further distinction is made between the two direction orthogonal to \hat{d} : \hat{d}_2 is the Cartesian vector orthogonal to \hat{d} , and \hat{d}_1 is orthogonal to both \hat{d} and \hat{d}_2 . $\vec{\xi}_{i+\hat{d}}$ is the value of $\vec{\xi}$ for the site at distance \vec{d} from site i .

By substituting the results of Table V and the appropriate values of $\vec{\xi}_i$ into Eqs. 3.7-3.9, we obtained the local harmonic coefficient A and the intersite coupling constants b_L , b_T , $d_L + d_{T1}$, d_{T2} and $f_L + 2f_T$ shown in Table VI. There was not enough information at the high symmetry \mathbf{q} points used to separate d_L from d_{T1} or f_L from f_T . As long as d_L , d_{T1} , f_L and f_T were all nonnegative, however, we found that the values chosen had little effect on the thermodynamic properties of our model, so we set $f_L = f_T$ and $d_L = d_{T1}$. Note that the local correction to the dipole-dipole energy decreases as the intersite distance increases, becoming smaller than the dipole-dipole interaction at third neighbors. While there is a tendency for the intersite interaction to approach the dipole-dipole form at large distances, there is still significant deviation from this form at third neighbor distance.

Next, consider the anharmonic terms to be included in the model Hamiltonian. Such terms are crucial for determining the thermodynamics of a system undergoing a mode-softening structural phase transition. Making an important simplifying approximation which has been previously applied in the study of GeTe¹² and perovskite oxides^{13–15}, we ignore multisite and higher-order pair interactions in our model Hamiltonian and include anharmonic terms only in the local distortion energy U_{la} . The Ge sites are centers of full cubic symmetry; thus the onsite energy expansion includes only cubic invariant terms. We truncate the expansion at eighth order, including all terms up to quartic order and the isotropic sixth and eighth order terms:

$$U_{la}/N = \frac{1}{N} \sum_i (B|\vec{\xi}_i|^4 + C(\xi_{ix}^4 + \xi_{iy}^4 + \xi_{iz}^4) + D|\vec{\xi}_i|^6 + E|\vec{\xi}_i|^8). \quad (3.10)$$

The coefficients B, C, D and E were obtained from a series of frozen phonon calculations at Γ , after subtracting the Γ point harmonic energy, $-1.6524 \text{ eV} |\vec{\xi}|^2$ (Table V). Various amplitudes of distortion $|\vec{\xi}|$ were applied in both the \hat{z} and $(\hat{x} + \hat{y} + \hat{z})/\sqrt{3}$ directions and a least squares fit to Eq. 3.10 was performed using the *ab initio* total energy results. The resulting coefficients are given in Table VI. A comparison of the frozen phonon and fitted results is shown in Figure 4(a). A contour plot of the equal energy surfaces of the fit is shown in Figure 4(b). The energy minima are located along the $[111]$ directions.

While the spin-like model obtained so far includes the necessary ingredients for a phase transition, the ground state symmetry of the crystal, degree of distortion and the nature of the phase transition all depend on magnitudes of both the strain (Eq. 2.6) and strain coupling terms (Eq. 2.7).⁴⁷ We include the effects of strain and strain coupling to lowest order. The symmetry adapted forms are:

$$U_{strain}/N = \frac{1}{2}C_{11} \sum_{\alpha} e_{\alpha\alpha}^2 + \frac{1}{2}C_{12} \sum_{\alpha \neq \beta} e_{\alpha\alpha} e_{\beta\beta} + \frac{1}{4}C_{44} \sum_{\alpha \neq \beta} e_{\alpha\beta}^2 \quad (3.11)$$

and

$$U_{strain \text{ coupling}}/N = \frac{g_0}{N} (\sum_{\alpha} e_{\alpha\alpha}) \sum_i |\vec{\xi}_i|^2 + \frac{g_1}{N} \sum_{\alpha} (e_{\alpha\alpha} \sum_i \xi_{i\alpha}^2) + \frac{g_2}{N} \sum_{\alpha < \beta} e_{\alpha\beta} \sum_i \xi_{i\alpha} \xi_{i\beta} \quad (3.12)$$

The variations in cell energy of uniformly strained Pb_3GeTe_4 structures, with Pulay corrections, are shown in Figure 5 for the following types of strain: uniform dilation ($e_{xx} = e_{yy} = e_{zz}$), tetragonal strain ($e_{xx} = e_{yy} = -e_{zz}/2$) and rhombohedral shear ($e_{xy} = e_{yx} = e_{xz} = e_{zx} = e_{yz} = e_{zy}$). Least squares fits to these results determine the elastic constants C_{11} , C_{12} and C_{44} shown in Table VI.

Finally, strain couplings were calculated by subtracting the energy at $\vec{\xi} = 0$ from various uniform fixed amplitude ($|\vec{\xi}| = 0.25$) distortions under various strains, using Eq. 3.12 to determine the form of the corresponding energy differences and finding the unknown coefficients via the linear parts of least-squares quadratic fits to each curve. The results are shown in Fig. 6. In Table VI, we present the values obtained for the three independent strain coupling parameters g_0 , g_1 and g_2 . As a check, further calculations were performed in which the amplitude of the LWF distortion was also varied. The results were consistent with the strain coupling parameters found.

The effect of strain on the energy of a Γ local polar distortion is shown in Figure 7, which is similar to Figure 4(b), except that the distortion energy is now minimized with respect to uniform strain. There are still 8 local minima along the $[111]$ directions. Their energies are 17 meV/cell lower, and corresponding values of $|\vec{\xi}_i|$ 0.035 larger than if the terms involving strain are neglected.

IV. FINITE TEMPERATURE SIMULATIONS

The model Hamiltonian constructed in the previous section is completely specified by

$$U(\{\vec{\xi}_i\}, \mathbf{e})/N = (U_0 + U_{lh} + U_{dd} + U_{sr} + U_{la} + U_{strain} + U_{strain\ coupling})/N, \quad (4.1)$$

where the individual contributions are given by Eqs. 3.1 and 3.6-3.12 and the parameters appear in Table VI. This model Hamiltonian applies to all ionic displacements believed to play a role in the structural phase transition and allows one to calculate T_c and other properties in the vicinity of the transition for the ordered Pb_3GeTe_4 system. We analyzed the

finite-temperature behavior using a classical “single flip” Metropolis Monte Carlo simulation. Three types of Monte Carlo steps were applied: (1) A “spin” $\vec{\xi}_i$ was chosen at random. A random vector located within a cube centered on the origin was added to the chosen spin vector. Acceptance ratios of about $1/e$ were obtained for a cube radius of $2\sqrt{kT}$, where kT is in eV. (2) A spin was chosen at random. The x , y and z components were independently multiplied by ± 1 with probability 0.5. This led to a great increase in simulation speed as the spins were able to overcome barriers between local energy minima. An acceptance ratio of about 0.3 was found for this step near T_c . (3) One strain component was chosen at random. A random number between $-\epsilon$ and $+\epsilon$ was added to this strain component. Acceptance ratios of about $1/e$ were obtained for cubic cells for $\epsilon = 0.15\sqrt{kT/L}$, where kT was in eV and L was the size of the cube edge in units of a .

We simulated an $L \times L \times L$ supercell of cubic Pb_3GeTe_4 , with $L = 10$, representing 8000 atoms. We determined mean total energies and lattice parameters as a function of temperature. At each temperature, the parameters were averaged over N_s Monte Carlo attempts for $N_c = 100$ cycles. The longest autocorrelation time for the $\mathbf{q} = (2\pi/L)\hat{z}$ Fourier component of the spin field was determined to estimate the decorrelation time τ at each temperature. For a proper ensemble average, $N_s N_c \gg \tau$. We generally selected N_s so that $N_s N_c \approx 20\tau$. From the root mean square deviation of the individual cycle averages, σ_{rms} , we can obtain an estimate of the *rms* error for the ensemble averaged quantities⁴⁸,

$$\sigma = \sqrt{1 + (\tau/N_s)^2}(\sigma_{rms})/(\sqrt{N_c - 1}). \quad (4.2)$$

We ran the simulations for a range of temperatures between 0K and 1000K. We began at 1000K, cooled to 0K and heated back up to test for hysteresis effects. At each temperature, the system was allowed to equilibrate before any sampling began.

At each temperature, the symmetry of the average cell was either cubic or rhombohedral to within statistical errors. Therefore the lattice parameter and the rhombohedral angle as a function of temperature are sufficient to give the unit cell as a function of temperature. The results are shown in Figure 8 and are consistent with a second order cubic-rhombohedral

phase transition at $T_c = 620\text{K}$. The error bars for certain temperatures very near T_c may be consistent with slight hysteresis, indicating a very weak first order transition. However, since this is observed in the temperature range where the effects of the periodic boundary conditions are significant, no firm conclusion can be reached. In any case, the hysteresis effect, if it exists, spans less than 10 degrees. Experiments on disordered $\text{Pb}_{1-x}\text{Ge}_x\text{Te}$ for small x show a continuous transition⁴ and give $T_c \approx 350\text{K}$ for $x = 0.25$. This apparent discrepancy in T_c will be discussed in detail in the next section.

The plot of lattice parameter versus temperature shows a discontinuous slope at T_c and a negative coefficient of thermal expansion below T_c . The model cannot be expected to obtain the right value for thermal expansion coefficient because it neglects anharmonic terms involving the normal modes complementary to the effective Hamiltonian subspace. The inclusion of additional modes should not alter the predicted *discontinuity* in the expansion coefficient, however, and a discontinuity of the right magnitude has indeed been observed experimentally in $\text{Pb}_{1-x}\text{Ge}_x\text{Te}$.⁴

V. DISCUSSION

In this section, we discuss further various features of our model Hamiltonian, compare the model with other systems and models, comment on the apparent discrepancy between our T_c and the experimental value, and discuss what the present calculations have taught us about generalizing to the case of *disordered* systems.

The harmonic part of our model is completely given by the normal mode dispersion curves. In Figure 9, these dispersion curves are shown for high symmetry paths in the Brillouin zone. Three features are particularly noteworthy: (1) Roughly speaking, there is a relatively flat branch at $\omega \approx 425\text{ cm}^{-1}$ and a relatively flat branch at $\omega \approx 600i\text{ cm}^{-1}$. This reflects the dominance of the longitudinal first neighbor dipole-dipole interaction and correction term b_L . (2) Although weaker than the first neighbor longitudinal interaction, the other interactions are crucial for determining the ground state structure. For example,

if the correction to the first neighbor transverse interaction, b_T , were zero, the most unstable modes would have symmetry $M_{1'}$ and the ground state would be antiferroelectric rather than ferroelectric. (3) The long-range dipole-dipole interaction leads to LO-TO splitting at Γ . The frequency of the TO mode at Γ is still negative, as opposed to the case of various perovskite ferroelectrics⁴⁹, where the LO mode corresponding to the soft TO mode generally has very high frequency. This is a consequence of the strength of the Ge off-centering instability in $\text{Pb}_{1-x}\text{Ge}_x\text{Te}$.

The form of our model Hamiltonian is that of interacting vectors on a cubic lattice. The same form of model Hamiltonian applies to perovskite ferroelectrics; thus the difference in phase transformation behavior of the different models can be related to the differences in the parameters and/or the number of vectors per unit cell. A comparative study of all the models to date is outside the scope of this paper; we will just compare the effects of strain coupling in our Pb_3GeTe_4 model and the PbTiO_3 model of Waghmare and Rabe.¹³ The effect of strain coupling in Pb_3GeTe_4 is much weaker than in PbTiO_3 . For each case, we compared the energy in the ground state of the corresponding model with the symmetric reference state energy. In Pb_3GeTe_4 , the distortion energy was -121 meV/cell, while strain and strain coupling contributed only -20 meV/cell. In PbTiO_3 on the other hand, the strain and strain coupling energy was -233 meV/cell at the ground state. Neglecting these terms, the distorted ground state was 120 meV/cell *higher* in energy than the reference state. The difference in the strength of strain coupling also makes the difference between a continuous phase transition in our Pb_3GeTe_4 model and a first-order phase transition in the PbTiO_3 model.^{13,47}

In the Ge off-centering model of $\text{Pb}_{1-x}\text{Ge}_x\text{Te}$ ^{7,8}, each Ge atom is displaced off-center in one of the 8 cubic $[111]$ directions. The cubic-rhombohedral phase transition is an order-disorder transition involving the *directions* of the displacements. Above T_c , the directions of the Ge atom displacements is disordered. There is no net polarization and the symmetry is cubic. Below T_c , the directions of the Ge atom displacements are ordered and lie predominantly along one axis, lowering the symmetry from cubic to rhombohedral and making the

system polar.

Our model, derived from first principles, essentially confirms the Ge off-centering model. It contains a local polar distortion (the LWF) dominated by Ge motion, whose energy minima are in directions where the Ge are displaced along the $[111]$ directions (Figure 4) in agreement with the off-centering model. To see if the phase transition in our model is order-disorder, we calculated the distribution of local distortion vectors at $T_c - 50\text{K}$ and $T_c + 50\text{K}$. The results are shown in Figure 10. Above T_c , there are distinct peaks in all eight $[111]$ directions, while below T_c , there is only a single peak in one of the $[111]$ directions, confirming the order-disorder nature of the transformation. We note here that EXAFS measurements of Islam and Bunker¹⁰ leave an ambiguity in the direction of displacements of the Ge atoms at low temperature. For a ground state with rhombohedral strain along the (111) direction, say, both (111) and $(\bar{1}\bar{1}\bar{1})$ local polar distortions lead to the same Ge-Te near neighbor pair distribution functions. In our model, the interactions between the local polar distortions have been determined and they are found to lead unequivocally to strictly ferroelectric ordering of these distortions.

EXAFS measurements¹⁰ show two peaks in the Ge-Te distribution function in $\text{Pb}_{1-x}\text{Ge}_x\text{Te}$. Only a displacement of Ge along one of the $[111]$ directions breaks the symmetry in a way that leads to two different Ge-Te near neighbor distances. Although the local polar distortion of our model involves motion of atoms other than the central Ge, the same result holds that only a local polar distortion along a $[111]$ direction leads to exactly two different Ge-Te distances. However, in our model, both the fact that the ionic displacement patterns corresponding to local polar distortion on different Ge atoms can overlap and the fact that the local polar distortions do not lie strictly along the $[111]$ directions (see Figure 10) makes it less certain that there is a two-peak Ge-Te distribution function. By transforming the $\{\vec{\xi}_i\}$ coordinates of our model back to ionic displacements via equation 2.12, we can calculate the first-neighbor Ge-Te distribution functions of our model. We show our results in Figure 10. There are two peaks, even above T_c , although there is significant overlap. These distribution functions do not incorporate the thermal noise of the neglected normal

modes, which would tend to further broaden the peaks; nonetheless, they are consistent with the experimental results showing two peaks.

Since the semi-empirical models of Katayama and Murase⁸ (KM) and of Yaraneri *et al.*⁹ are based upon Ge ions tunneling between (111) and ($\overline{1}\overline{1}\overline{1}$) positions, in apparent contradiction with our results showing one preferred position below T_c , we have investigated this issue more carefully. Extrapolating our model to lower Ge concentrations by setting the dipole-dipole interactions to be that corresponding to an fcc dipole lattice at the given density and interpolating the lattice parameter between the LDA values for PbTe and Pb₃GeTe₄ via Vegard's law, we obtain a rough estimate of composition $x \approx 0.05$, below which there are two wells in the potential along the (111) line. Using a different analysis, Katayama and Murase estimated the range of validity of their model to be $x < 0.1$.

Although our model is classical, it sheds some light on quantum tunneling phenomena in the Pb_{1-x}Ge_xTe system at small x by providing a potential energy surface for Ge motion. In Figure 11(a), we show the potential energy surface for Ge motion in cubic Pb₃GeTe₄ at zero temperature. There is only a single deep well for the Ge ion and thus no quantum tunneling. A more relevant potential energy surface is that for a single Ge impurity in PbTe. While our calculations were performed on a structure with 25% Ge, a crude extrapolation to the isolated impurity case is possible by (1) setting all Ge-Ge interaction terms equal to zero and (2) setting the lattice parameter to the value for pure PbTe. When this is done, the potential energy surface for Ge atom motion is that shown in Figure 11(b). There are now eight wells with minima along cubic [111] directions, about 7 meV deep with respect to the centered position and with 1 meV barriers between wells. The zero-point vibrational energy of a Ge atom in this potential is about 20 meV, so it would not be localized in a single well. At some nonzero concentration of Ge impurities, we expect the Ge-Ge off-centering interactions to overcome the zero-point vibrational motion leading to an ordered rhombohedral ground state.

The KM model includes not only Ge off-centering, but coupling of Ge motion to the PbTe transverse optical phonons. In our calculation of normal modes, the coupling of Ge motion to

other ionic motions is given in the dynamical matrix, which is then diagonalized. Compared to the KM model, we both reduce the number of degrees of freedom and incorporate normal modes that are more appropriate for a material containing substitution. Consider our Γ_{15} eigenmode (Table II). All Pb motion in this eigenmode is in the opposite direction of all Te motion, exactly as would be the case of the zone center PbTe TO phonon. The motion of one Te atom, however, is much larger in magnitude than all other Pb and Te motions, reflecting the importance of localization phenomena.

It is instructive to compare our results for Pb_3GeTe_4 with similar results for pure PbTe. Linear response calculations on PbTe were carried out using the experimental rocksalt structure as the reference structure and the LDA lattice parameter. All normal modes are stable, consistent with the experimental fact that PbTe is cubic down to zero temperature.^{4,6} It is also consistent with the fact that the instabilities in ternary Pb_3GeTe_4 are associated with the Ge ions.

For pure PbTe, we obtain Born effective charges of +5.84 for Pb and -5.84 for Te and an electronic dielectric constant of 33.0. These are in excellent agreement with the experimental values of $Z^* = \pm 6.0$ and $\epsilon_\infty = 32.8$ ⁴³ and suggest that our values for Pb_3GeTe_4 are also reliable. Our calculations show that ϵ_∞ for Pb_3GeTe_4 is about 40% higher than for PbTe. When Ge is substituted for Pb, the Pb effective charge changes little and remains nearly isotropic. The Ge effective charge itself is significantly larger than that for the Pb it replaces. The Te(2) Z^* also changes substantially and becomes markedly anisotropic. An analogous anisotropy has been observed for the oxygen Z^* in ABO_3 perovskite ferroelectrics.^{49,50} It is interesting that the two Z^* components of highest magnitude are associated with the two most significant ionic displacements in the LWF, namely Ge off-centering along with axial motion of the first neighbor Te ions.

The values of the Born effective charges (and ϵ_∞) in Pb_3GeTe_4 do not remain constant as the structure distorts from its reference structure to its ground state. We set the structure of Pb_3GeTe_4 to the ground state of our model ($e_{\alpha\alpha} = 6.37 \times 10^{-3}$; $e_{\alpha\beta} = 6.03 \times 10^{-3}$, $\alpha \neq \beta$; $\vec{\xi} = (0.255, 0.255, 0.255)$) and recalculated the Born effective charge tensors. The results

are shown in Table VII. The magnitude of the Born effective charges are generally smaller in the distorted state, sometimes much smaller. In particular, Z^* for Ge along (111) goes from +8.02 to +1.52; the *electronic* contribution to Z^* goes from positive to negative. Previous studies have shown similar, but smaller decreases in magnitudes of Z^* in BaTiO_3 ⁵⁰ and KNbO_3 ⁵¹ as the structure is distorted. A common trend is that the atoms with the largest relative motion in the structural instability have the largest changes in Z^* . The magnitude of ϵ_∞ also decreased substantially as the structure distorted. A similar, but relatively smaller, decrease has been calculated for KNbO_3 ⁵¹.

The large difference between T_c for our Pb_3GeTe_4 model and the experimental T_c for the disordered system at the same composition merits discussion. The first source for the discrepancy is the approximations used in the first-principles energy calculations. Approximations in the *ab initio* calculations include the use of pseudopotentials, LDA, finite k-point sampling, a finite cutoff energy and a finite real-space grid for charge density. The second source for the discrepancy is the net effect of the neglected anharmonic effects, which may be important in Pb_3GeTe_4 because the relative displacements of the ions is so large (order 0.5 Å). For example, the dependence of Z^* on distortion discussed in the previous paragraph will lead to a nonlinear dependence of \mathbf{P}_i on $\vec{\xi}_i$, which in turn will lead to anharmonic intersite interactions. Such anharmonic effects could either raise or lower T_c and are worth further study. The third source for the discrepancy is our use of the LDA lattice parameter rather than the (unknown) experimental one.⁵² Typically, *ab initio* phonon calculations using experimental lattice parameters are more accurate than those based on the LDA lattice parameters.⁵² In section 3, we estimated that the LDA lattice parameter a for Pb_3GeTe_4 is about 0.5% smaller than the experimental value, so more accurate results might be obtained by raising a . In general, raising the lattice parameter will “soften” the phonons and thus raise T_c ; in the present case, this would increase the discrepancy between our T_c and the experimental value.

Finally, there is the problem of extending the results for an ordered structure to those for a disordered alloy. We have, in effect, considered only one term in Eq. 2.1, which is not

in fact “typical”. For example, in the cubic configuration no relaxation is possible. Other configurations at the same composition do allow relaxation. We have preliminary *ab initio* results that show that the relaxation in disordered $\text{Pb}_{1-x}\text{Ge}_x\text{Te}$ is dominated by a 0.11 to 0.14 Å inward displacement of each Te in the first neighbor shell of each Ge ion, where such relaxation does not conflict with the relaxation about a second Ge ion. Such relaxation alone lowers the energy per Pb_3GeTe_4 unit as much as 20 meV per atom with respect to the undistorted cubic structure. Locally, the relaxation mimics a decrease of the lattice parameter, which should “harden” the unstable Ge-dominated modes and thus decrease T_c .

The large energy differences between different configurations of Pb_3GeTe_4 upon relaxation shows the necessity of including different chemical configurations in order to correctly model the structural phase transition in the disordered system. This is similar to the case of alloy phase diagrams⁵³, where order-disorder transitions predominate. There, it has been shown that lattice entropy effects must be included to obtain correct transition temperatures for order-disorder transitions.^{54,55} Here, we need to include configurational entropy in order to study a structural phase transition.

The situation for $\text{Pb}_{1-x}\text{Ge}_x\text{Te}$ is complicated by the existence of a miscibility gap, with the peak of the exsolution dome at about 840 K⁴. For $x = 0.25$, as in this work, phase separation to Ge-rich and Pb-rich phases occurs at about 770 K⁴, although a mixed phase of this composition that is metastable at low temperatures can be obtained by rapid quenching⁴. Thus, the experimental result of $T_c \approx 350\text{K}$ for the structural phase transition in $\text{Pb}_{0.75}\text{Ge}_{0.25}\text{Te}$ actually applies to a metastable compound and the thermodynamic theory for the disordered compound is complicated by the fact that the equilibrium partition function (Eq. 2.1) does not apply.

Finally, we discuss the form of the model that should describe disordered $\text{Pb}_{1-x}\text{Ge}_x\text{Te}$. For each configuration in Eq. 2.1, it is possible in principle to repeat the procedure used in this work to develop a configuration specific model. Based on the Ge off-centering picture, we make the following conjectures about the nature of all such models. (1) There is a basis for all unstable modes that involves a vector LWF centered on each Ge. (2) The displacement

pattern corresponding to each LWF will be strongly localized. (3) The interactions between local polar distortions centered on different Ge will favor ferroelectric ordering.

Given enough models for individual configurations, it should be possible to extract a “supermodel” that applies to all $\text{Pb}_{1-x}\text{Ge}_x\text{Te}$ configurations. In the same way that energy for a disordered alloy can be given in terms of a cluster expansion⁵³, the values of the model parameters could also be given in terms of cluster expansions. Work is in progress to develop models for other $\text{Pb}_{1-x}\text{Ge}_x\text{Te}$ configurations and to incorporate the effects of relaxation into these models.

VI. CONCLUSIONS

As a first step towards a first-principles study of the effect of substitutional disorder in $\text{Pb}_{1-x}\text{Ge}_x\text{Te}$, we have developed a model Hamiltonian for an ordered Pb_3GeTe_4 system. We have determined the parameters in this model from *ab initio* calculations. From a classical Monte Carlo simulation, T_c was found to be about 620K. Comparison of the present results with those obtained for other configurations will demonstrate how transferable the parameters of the model Hamiltonian for this ordered supercell are to other configurations, show how much T_c depends on configuration. and allow a model for the disordered system to be developed.

VII. APPENDIX

The use of a plane wave basis set and periodic boundary conditions in an *ab initio* calculation introduces two kinds of error. The first is due to the finite energy cutoff for the plane waves; the second is due to the discretization of wavevectors that is a result of using a finite periodic cell in real space. In this paper, we use Pulay corrections to compensate for the second source of error.

The specific method for applying Pulay corrections used here was taken from Rignanese *et al.*³⁶. In this method, the density functional total energy E_{tot} of a periodic system at

fixed volume V_0 is measured at several cutoff energies E_{cut} and treated as a function of the average number of plane waves per \mathbf{k} point, \overline{N}_{PW} at those values of E_{cut} . Rignanese *et al.* suggest using cutoff energies of E_{cut} (the fixed value for a set of calculations of different cells), $E_{cut} - 3\%$ and $E_{cut} + 3\%$ and then fitting through the resulting total energies $E_{tot}[\overline{N}_{PW}, V_0]$ via the following function:

$$E_{tot}[\overline{N}_{PW}, V_0] = E_{tot}^{inf} + \exp(a_0 + a_1 \overline{N}_{PW}). \quad (7.1)$$

Finally, the results obtained for the *single* cell volume V_0 are used to determine the Pulay corrections to total energy for *any* cell volume V_1 via the correction:

$$E_{tot}^c[E_{cut}, V_1] \sim E_{tot}^d[E_{cut}, V_1] + E_{tot}\left[\frac{V_0}{V_1} \overline{N}_{PW}^c(E_{cut}, V_1), V_0\right] - E_{tot}\left[\frac{V_0}{V_1} \overline{N}_{PW}^d(E_{cut}, V_1), V_0\right] \quad (7.2)$$

$E_{tot}^d[E_{cut}, V_1]$ is the total energy measured without corrections. \overline{N}_{PW}^d is the corresponding average number of plane waves per \mathbf{k} point. \overline{N}_{PW}^c is the “continuous” number of plane waves at E_{cut} , determined by multiplying the density of states in reciprocal space by the volume of the sphere containing plane waves of energy less than E_{cut} and is given by

$$\overline{N}_{PW}^c(E_{cut}, V) = \frac{V}{6\pi^2} (2E_{cut})^{3/2}, \quad (7.3)$$

when V and E_{cut} are in atomic units. From the value of $\overline{N}_{PW}^c(E_{cut}, V_1)$ obtained, the corrected total energy $E_{tot}^c[E_{cut}, V_1]$ can be computed.

By measuring the total energy of Pb_3GeTe_4 at $a = 6.375 \text{ \AA}$ and PbTe at $a = 6.275 \text{ \AA}$ at $E_{cut} = 291, 300$ and 309 eV , the following fitting forms were obtained:

$$\text{PbTe} : E_{tot}[\overline{N}_{PW}, V_0 = 259.05 \text{ \AA}^3] = -1296.5850 + 6.244 \exp(-1.95610^{-4} \overline{N}_{PW}^d) \quad (7.4)$$

$$\text{Pb}_3\text{GeTe}_4 : E_{tot}[\overline{N}_{PW}, V_0 = 247.05 \text{ \AA}^3] = -1308.4464 + 8.452 \exp(-9.30710^{-5} \overline{N}_{PW}^d)$$

These results were used to correct all the CASTEP 2.1 total energy results used in this article. From the expression (7.4) for E_{tot} , and the value of $\overline{N}_{PW}^d = 2911.75$ corresponding to our calculation for Pb_3GeTe_4 at $a = 6.275 \text{ \AA}$, we obtained $E_{tot} \equiv U_0/N = -1302.1725 \text{ eV}$.

VIII. ACKNOWLEDGEMENTS

This work was supported by ONR N00014-91-J-1247. We thank Philippe Ghosez and Umesh Waghmare for useful discussions and helpful assistance. We thank Alex Elliott and Nicola Hill for their comments on the manuscript.

REFERENCES

- ¹ V. V. Lemanov, E. P. Smirnova, P. P. Syrnikov and E. A. Tarakanov, *Phys. Rev. B* **54**, 3151 (1996).
- ² G. Shirane, K. Suzuki and A. Takeda, *J. Phys. Soc. Japan* **7**, 12 (1952).
- ³ E. G. Fesenko, V. V. Eremkin and V. G. Smotrakov, *Sov. Phys. Solid State* **28**, 181 (1986).
- ⁴ D. K. Hohnke, H. Holloway and S. Kaiser, *J. Phys. Chem. Solids* **33**, 2053 (1972).
- ⁵ K. Schubert and H. Fricke, *Z. Metallkunde* **44**, 457 (1953).
- ⁶ S. Takaoka and K. Murase, *Phys. Rev. B* **20**, 2823 (1979).
- ⁷ Yu. A. Logachev and B. Ya. Moizhes, *Sov. Phys. Solid State* **19**, 1635 (1977). (*Fiz. Tverd. Tela* (Leningrad) **19**, 2793 (1977)).
- ⁸ S. Katayama and K. Murase, *Solid State Communications* **36**, 707 (1980).
- ⁹ H. Yaraneri, A. D. C. Grassie, H. Yusheng and J. W. Loram, *J. Phys. C: Solid State Phys.* **14**, L441 (1981).
- ¹⁰ Q. T. Islam and B. A. Bunker, *Phys. Rev. Lett.* **59**, 2701 (1987).
- ¹¹ A. S. Barker Jr. and A. J. Sievers, *Rev. Mod. Phys.* **47** Suppl. No. 2, S118 (1975).
- ¹² K. M. Rabe and J. D. Joannopoulos, *Phys. Rev. Lett.* **59**, 570 (1987).
- ¹³ K. M. Rabe and U. V. Waghmare, *Ferroelectrics* **164**, 15 (1995); U. V. Waghmare and K. M. Rabe, *Phys. Rev. B* **55**, 6161 (1997).
- ¹⁴ U. V. Waghmare and K. M. Rabe, to be published in *J. Phys. Chem. Solids*.
- ¹⁵ W. Zhong, D. Vanderbilt, and K. M. Rabe, *Phys. Rev. Lett.* **73**, 1861 (1994); *Phys. Rev. B* **52**, 6301 (1995).
- ¹⁶ W. Zhong, D. Vanderbilt, R. D. King-Smith and K. M. Rabe, *Ferroelectrics* **164**, 291

- (1995).
- ¹⁷ W. Zhong and D. Vanderbilt, *Phys. Rev. B* **53**, 5047 (1996).
- ¹⁸ H. Krakauer, C. Z. Wang, R. Yu, K. M. Rabe and U. V. Waghmare, unpublished.
- ¹⁹ K. M. Rabe and U. V. Waghmare, *Phys. Rev. B* **52**, 13236 (1995).
- ²⁰ K. M. Rabe and U. V. Waghmare, *Ferroelectrics* **136**, 147 (1992); *Ferroelectrics* **151**, 59 (1994).
- ²¹ J. des Cloizeaux, *Phys. Rev.* **135**, A698 (1964).
- ²² G. B. Bachelet, D. R. Hamann and M. Schlüter, *Phys. Rev. B* **26**, 4199 (1982).
- ²³ L. Kleinman and D. M. Bylander, *Phys. Rev. Lett.* **48**, 1425 (1982).
- ²⁴ P. E. Blöchl, *Phys. Rev. B* **41**, 5414 (1990).
- ²⁵ X. Gonze, P. Käckell and M. Scheffler, *Phys. Rev. B* **41**, 12264 (1990).
- ²⁶ X. Gonze, *Phys. Rev. B* **44**, 8503 (1991).
- ²⁷ M. C. Payne, X. Weng, B. Hammer, G. Francis, I. Stich, U. Bertram, A. de Vita, J. S. Lin, A. Qteish and V. Milman, “CASTEP 2.1”, Cavendish Laboratory, University of Cambridge (1991).
- ²⁸ M. C. Payne, M. P. Teter, D. C. Allan, T. A. Arias and J. D. Joannopoulos, *Rev. Mod. Phys* **64**, 1045 (1992).
- ²⁹ W. Kohn and L. J. Sham, *Phys. Rev.* **140**, A1133 (1965).
- ³⁰ J. Perdew and A. Zunger, *Phys. Rev. B* **23**, 5048 (1981).
- ³¹ D. M. Ceperley, *Phys. Rev. B* **18** (1978) 3126; D. M. Ceperley and B. J. Alder, *Phys. Rev. Lett.* **45**, 566 (1980).
- ³² H. J. Monkhorst and J. D. Pack, *Phys. Rev. B* **13**, 5188 (1976).

- ³³ S. Baroni, P. Giannozzi and A. Testa, *Phys. Rev. Lett.* **58**, 1861 (1987).
- ³⁴ P. Giannozzi, S. de Gironcoli, P. Pavone and S. Baroni, *Phys. Rev. B* **43**, 7231 (1991).
- ³⁵ X. Gonze, D. C. Allan and M. P. Teter, *Phys. Rev. Lett.* **68**, 3603 (1992).
- ³⁶ G.-M. Rignanese, P. Ghosez, J.-C. Charlier, J.-P. Michenaud and X. Gonze, *Phys. Rev. B* **52**, 8160 (1995).
- ³⁷ W. Lugscheider, H. Ebel and G. Langer, *Z. Metallkunde* **56**, 851 (1965).
- ³⁸ T. B. Zhukova and A. I. Zaslavskii, *Soviet Physics- Crystallography* **12** 28 (1967).
- ³⁹ C. Filippi, D. J. Singh, and C. J. Umrigar, *Phys. Rev. B* **50**, 14947 (1994).
- ⁴⁰ The normal modes are labeled according to the convention of F. Bassani, G. Pastori Paravicini and R. A. Ballinger, *Electronic States and Optical Transitions in Solids*, Pergamon Press, New York, 1975, with a Ge atom at the origin.
- ⁴¹ The reciprocal space equivalent of this sum is given by R. M. Pick, M. H. Cohen and R. M. Martin, *Phys. Rev. B* **1**, 910 (1970) and by Reference 49.
- ⁴² X. Gonze and Ch. Lee, unpublished. An additional method is given for partitioning the missing charge among the ions.
- ⁴³ E. Burstein, A. Pinczuk and R. F. Wallis, in *Proc. Conf. Physics of Metals and Narrow Gap Semiconductors*, eds. D. L. Carter and R. T. Bate, New York, Pergamon, p. 251 (1970).
- ⁴⁴ P. B. Littlewood, *J. Phys. C* **12**, 4441 (1979); *J. Phys. C* **12**, 4459 (1979); *J. Phys. C* **13**, 4855 (1980); *CRC Crit. Rev. in Solid State and Mat. Sci.* **11**, 229 (1984).
- ⁴⁵ K. Murase and S. Sugai, *Solid State Communications* **32**, 89 (1979).
- ⁴⁶ Z. H. Levine and D. C. Allan, *Phys. Rev. Lett.* **63**, 1719 (1989).
- ⁴⁷ U. V. Waghmare and K. M. Rabe, *Phil. Trans. R. Soc. Lond. A* **354**, 2897 (1996).

- ⁴⁸ K. Binder, in *Phase Transitions and Critical Phenomena*, eds. C. Domb and M. S. Green, (New York: Academic Press) (1976).
- ⁴⁹ W. Zhong, R. D. King-Smith and D. Vanderbilt, *Phys. Rev. Lett.* **72**, 3618 (1994).
- ⁵⁰ P. Ghosez, X. Gonze, P. Lambin and J.-P. Michenaud, *Phys. Rev. B* **51**, 6765 (1995).
- ⁵¹ C.-Z. Wang, R. Yu, and H. Krakauer, *Phys. Rev. B* **54**, 11161 (1996).
- ⁵² M. T. Yin and M. L. Cohen, *Phys. Rev. B* **26**, 3259 (1982).
- ⁵³ J. W. D. Connolly and A. R. Williams, *Phys. Rev. B* **27**, 5169 (1983).
- ⁵⁴ A. Silverman, A. Zunger, R. Kalish and J. Adler, *J. Phys.: Condens. Matter* **7**, 1167 (1995).
- ⁵⁵ G. D. Garbulsky and G. Ceder, *Phys. Rev. B* **53**, 8993 (1996).
- ⁵⁶ International Union of Crystallography, *International Tables for Crystallography Vol. A: Space Group Symmetry*, T. Hahn, ed. (Boston: D. Riedel Pub. Company) (1983).

FIGURES

FIG. 1. Crystal structures of the observed phases of pure GeTe. Eight atom regions are shown for (a) the high-temperature rocksalt structure and (b) the low-temperature rhombohedral structure, which is related to (a) by a rhombohedral lattice distortion and a relative displacement of the sublattices, shown by arrows. Both distortions are greatly exaggerated for clarity.

FIG. 2. The high-symmetry reference structure of the ordered cubic Pb_3GeTe_4 eight-atom unit cell, produced by replacing a cubic superlattice of Pb ions (striped circles) in the PbTe rocksalt structure with Ge ions (solid circles).

FIG. 3. The z component of the estimated lattice Wannier function of cubic Pb_3GeTe_4 (doubled for clarity). Only ions with displacements greater than 0.1 times the displacement of the central Ge ion are shown. Note that the unit cell outlined is translated with respect to that in Figure 2.

FIG. 4. (a) Comparison of frozen phonon and fitted results for the unstable Γ mode subspace energy; strain fixed at zero. (b) Contour plot of $1\bar{1}0$ plane cross section of eighth order expansion of unstable Γ mode subspace energy. The contour interval is 20 meV and the grid spacing is 0.2.

FIG. 5. Energy vs. strain for (a) uniform dilation ($e_{xx} = e_{yy} = e_{zz}$), (b) tetragonal strain ($e_{xx} = e_{yy} = -e_{zz}/2$) and (c) rhombohedral strain ($e_{xy} = e_{xz} = e_{yz}$).

FIG. 6. Energy change due to local polar distortion of amplitude 0.25 on strained cells. (a) uniform dilation; $\vec{\xi} = |\vec{\xi}|\hat{z}$, (b) tetragonal strain; $\vec{\xi} = |\vec{\xi}|\hat{z}$, (c) rhombohedral strain; $\vec{\xi} = |\vec{\xi}|(\hat{x} + \hat{y} + \hat{z})/\sqrt{3}$.

FIG. 7. Contour plot of $1\bar{1}0$ plane cross section of unstable Γ mode subspace energy, minimized with respect to uniform strain. The contour interval and grid spacing are the same as in Figure 4.

FIG. 8. Result of Monte Carlo simulations. (a) Rhombohedral strain and (b) lattice parameter versus temperature. The results are consistent with a second order phase transition with T_c near 620 K.

FIG. 9. Phonon dispersion relations for the cubic Pb_3GeTe_4 model Hamiltonian.

FIG. 10. Distribution of $\vec{\xi}$ in Monte Carlo simulation. (a) Contour plot in $1\bar{1}0$ plane at $T_c+50\text{K}$. (b) Same as (a), at $T = T_c-50\text{K}$. (c) First neighbor Ge-Te distribution function at $T = T_c+50\text{K}$. (d) Same as (c) for $T = T_c-50\text{K}$. Compare (a) with figure 4(b). The eight $[111]$ directions are preferred for local distortions, even above T_c , in agreement with the Ge off-centering picture.

FIG. 11. (a) Potential energy surface seen by single Ge ion at $T = 0$ in Pb_3GeTe_4 model (contour interval 50 meV). (b) Potential energy surface seen by isolated Ge impurity in PbTe , based on extrapolation of our model (contour interval 5 meV).

TABLES

TABLE I. Ab initio frequencies (in cm^{-1}) of selected normal modes in cubic Pb_3GeTe_4 . The frequencies for optical Γ_{15} modes are for the transverse modes.

Symmetry Label:	Γ_{15}	Γ_{25}	$X_{1'}$	$X_{5'}$	$M_{1'}$	$M_{5'}$	R_{15}
	648 i	176	478	593 i	547 i	395	429
	0	630	518	163	315	603	437
	195		721	308		688	683
	292			622		736	
	518						
	662						

TABLE II. Displacements (in \AA) associated with all symmetry-independent modes incorporated into the model Hamiltonian. The periodicity of each mode listed except Γ_{15} is longer than the primitive cell and involves the opposite motion of some ions in neighboring cells.

Mode	Γ_{15}	$X_{1'}$	$X_{5'}$	$M_{1'}$	$M_{5'}$	R_{15}
ω (cm^{-1})	648 i	478	593 i	547 i	395	429
\mathbf{q} ($2\pi/a$)	(0,0,0)	(0,0,0.5)	(0,0.5,0)	(0.5,0.5,0)	(0,0.5,0.5)	(0.5,0.5,0.5)
\mathbf{u} (Ge(0,0,0))	0.8878 \hat{z}	0.8258 \hat{z}	0.8835 \hat{z}	0.8654 \hat{z}	0.8207 \hat{z}	0.8578 \hat{z}
\mathbf{u} (Te(0,0,0.5))	-0.4467 \hat{z}	0	-0.4668 \hat{z}	-0.5010 \hat{z}	0	0
\mathbf{u} (Te(0,0.5,0))	-0.0575 \hat{z}	0.0680 \hat{z}	0	0	0	0
\mathbf{u} (Te(0.5,0,0))	-0.0575 \hat{z}	0.0680 \hat{z}	-0.0318 \hat{z}	0	0.0555 \hat{z}	0
\mathbf{u} (Pb(0.5,0.5,0))	0.0156 \hat{z}	-0.5556 \hat{z}	0	0	0	0
\mathbf{u} (Pb(0.5,0,0.5))	0.0284 \hat{z}	0	0.0237 \hat{z}	0	0	-0.3569 \hat{x}
\mathbf{u} (Pb(0,0.5,0.5))	0.0284 \hat{z}	0	0	0	0.5684 \hat{y}	-0.3569 \hat{y}
\mathbf{u} (Te(0.5,0.5,0.5))	-0.0611 \hat{z}	0	0	0	-0.0163 \hat{y}	0

TABLE III. Ionic displacement pattern corresponding to z component of estimated lattice Wannier function $w_{z\mathbf{R}}$ for c-Pb₃GeTe₄. The lattice Wannier function transforms according to the Γ_{15} representation for point group O_h with center R . Orbits of equivalent atoms for $w_{z\mathbf{R}}$ are labeled according to the *International Tables*⁵⁶ convention for point group $4/mmm$. Components whose values are 0 vanish by symmetry, while those whose values are 0.0 are only zero by approximation.

Atom	$\mathbf{r}_i - \mathbf{R}$ (units of a)	Multiplicity (orbit)	\mathbf{u} (Å)
Ge	(0,0,0)	1	(0, 0, 0.8557)
Te	(0,0,0.5)	2(a)	(0, 0, -0.2352)
Ge	(0,0,1)	2(a)	(0, 0, 0.0122)
Te	(0.5,0,0)	4(c)	(0, 0, 0.0043)
Pb	(0.5,0,0.5)	8(f)	(0.1165, 0, 0.0065)
Te	(0.5,0,1)	8(f)	(0, 0, -0.0133)
Pb	(0.5,0.5,0)	4(b)	(0, 0, -0.0675)
Te	(0.5,0.5,0.5)	8(e)	(-0.0020, -0.0020, -0.0076)
Pb	(0.5,0.5,1)	8(e)	(0.0, 0.0, 0.0357)
Ge	(1,0,0)	4(c)	(0, 0, -0.0006)
Te	(1,0,0.5)	8(f)	(0.0, 0, 0.0034)
Ge	(1,0,1)	8(f)	(0.0, 0, 0.0017)
Te	(1,0.5,0)	8(d)	(0, 0, -0.0008)
Pb	(1,0.5,0.5)	16(g)	(0.0, 0.0128, 0.0003)
Te	(1,0.5,1)	16(g)	(0.0, 0.0 - 0.0012)
Ge	(1,1,0)	4(b)	(0, 0, 0.0009)
Te	(1,1,0.5)	8(e)	(0.0, 0.0, -0.0004)
Ge	(1,1,1)	8(e)	(0.0, 0.0, -0.0009)

TABLE IV. Born effective charges for cubic Pb_3GeTe_4 . For Ge and Te(1), Z^* is isotropic, while for Pb and Te(2), the parallel and perpendicular components refer to the local tetragonal axis.

Species	Z_{\parallel}^*	Z_{\perp}^*
Pb	+6.15	+6.06
Ge	+8.02	+8.02
Te(1)	-5.82	-5.82
Te(2)	-7.73	-6.37

TABLE V. Harmonic energies of effective Hamiltonian modes ($|\vec{\xi}| = 1$ on each Ge site). Units are eV per unit cell. Displacements of ions are given in Table II. The energy for Γ_{15} was determined via a frozen phonon calculation, the others are determined via nonzero \mathbf{q} linear response.

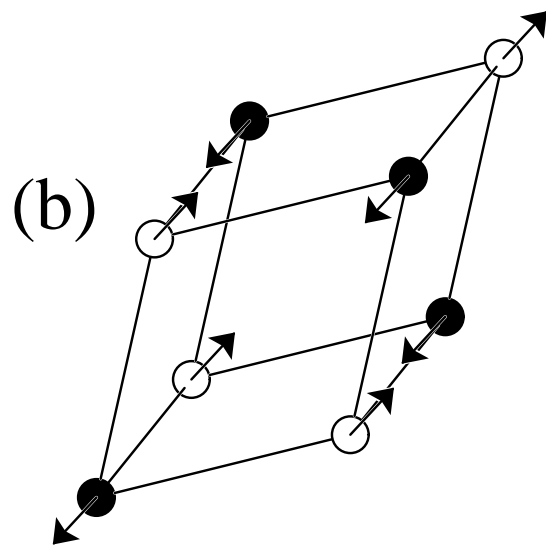
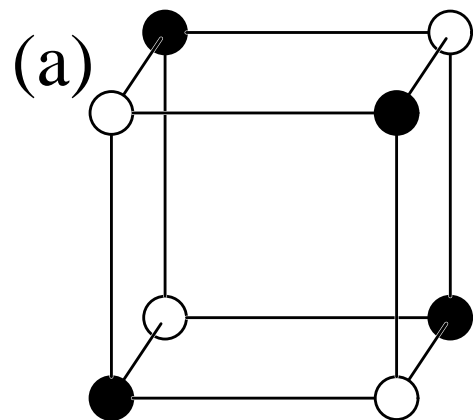
Mode	U_{harm}	U_{dipole}	U_{sr}	Energy via Eqs. 3.7-3.9
Γ_{15}	-1.652	-0.383	-1.269	$A + b_L + 2 b_T + 2 (d_L + d_{T1}) + 2 d_{T2} + 4 (f_L + 2 f_T)/3$
$X_{1'}$	1.220	0.885	0.335	$A - b_L + 2 b_T - 2 (d_L + d_{T1}) + 2 d_{T2} - 4 (f_L + 2 f_T)/3$
$X_{5'}$	-1.387	-0.443	-0.944	$A + b_L - 2 d_{T2} - 4 (f_L + 2 f_T)/3$
$M_{1'}$	-1.206	-0.489	-0.717	$A - b_L - 2 d_{T2} + 4 (f_L + 2 f_T)/3$
$M_{5'}$	0.844	0.245	0.599	$A + b_L - 2 b_T - 2 (d_L + d_{T1}) + 2 d_{T2} + 4 (f_L + 2 f_T)/3$
R_{15}	0.927	0.000	0.927	$A - b_L - 2 b_T + 2 (d_L + d_{T1}) + 2 d_{T2} - 4 (f_L + 2 f_T)/3$

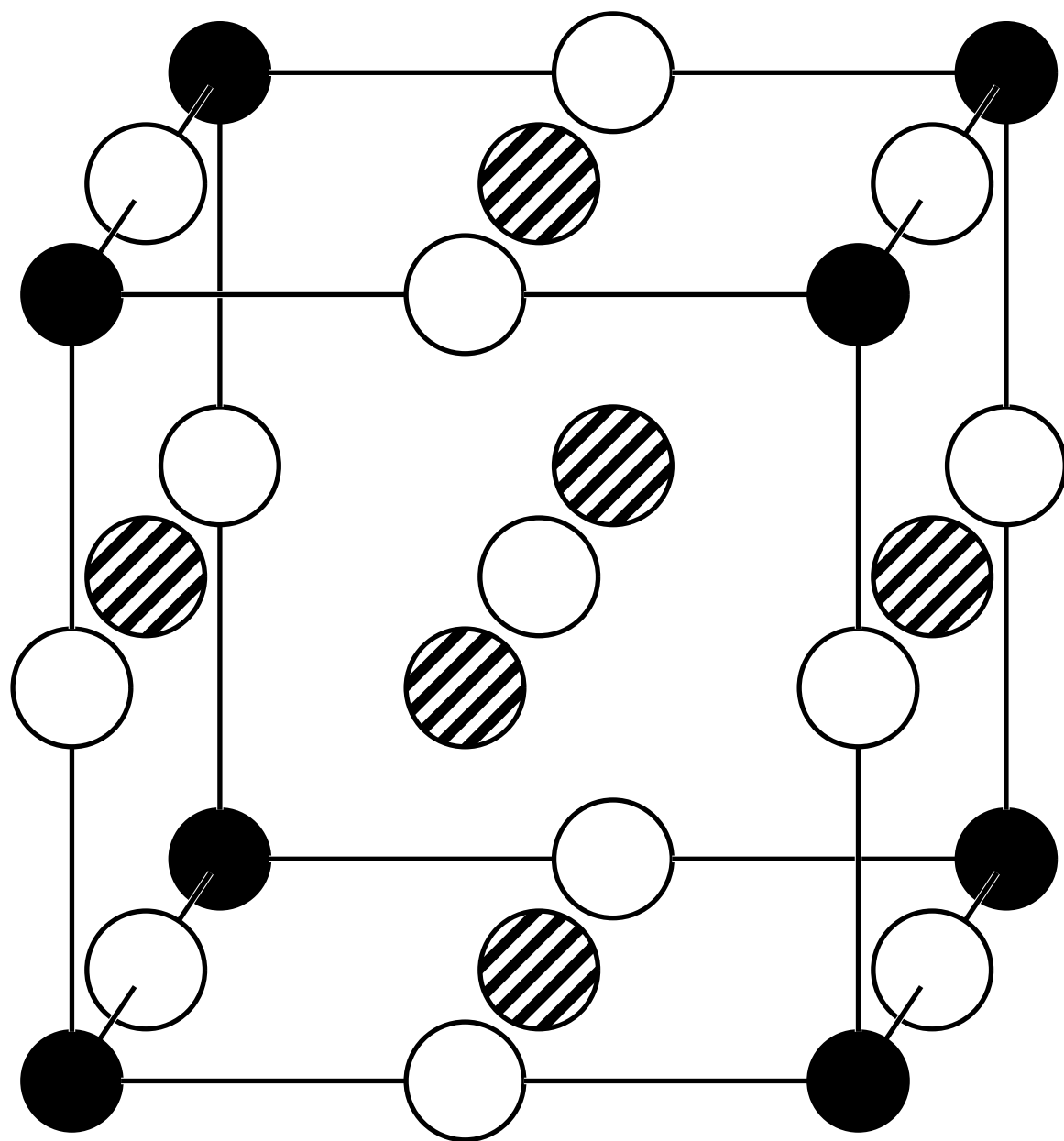
TABLE VI. Parameters in the effective Hamiltonian for Pb_3GeTe_4 (units of eV per unit cell).

A	-0.1765	b_L	-0.7922	C_{11}	215.8
B	4.501	b_T	-0.2148	C_{12}	9.374
C	6.165	$d_L + d_{T1}$	0.0766	C_{44}	108.1
D	-7.263			g_0	-3.50
E	4.239	d_{T2}	-2.98×10^{-2}	g_1	-12.4
Z^*	12.10	$f_L + 2f_T$	2.55×10^{-2}	g_2	-9.99
ϵ_∞	46.7	a	6.275 Å		

TABLE VII. Born effective charges and ϵ_∞ for ground state of cubic Pb_3GeTe_4 . Atomic positions are given to the nearest tenth. The principal directions are given by the subscripts. They are exact by symmetry for Ge, Te(1) and ϵ_∞ , but only approximate for Pb and for Te(2). The corresponding values for the high symmetry reference structure are given in Table IV and shown here in parentheses.

Pb (0.0,0.0,0.5) Z^*	+5.86 ₀₀₁ (6.15)	+5.84 _{1$\bar{1}$0} (6.06)	+4.98 ₁₁₀ (6.06)
Ge (0.0,0.0,0.0) Z^*	+1.52 ₁₁₁ (8.02)	+3.89 _{1$\bar{1}$0} (8.02)	+3.89 _{11$\bar{2}$} (8.02)
Te(1) (0.5,0.5,0.5) Z^*	-5.67 ₁₁₁ (-5.82)	-5.82 _{1$\bar{1}$0} (-5.82)	-5.82 _{11$\bar{2}$} (-5.82)
Te(2) (0.5,0.5,0.0) Z^*	-3.65 ₀₀₁ (-7.73)	-5.00 _{1$\bar{1}$0} (-6.37)	-5.42 ₁₁₀ (-6.37)
ϵ_∞	31.0 ₁₁₁ (46.7)	30.9 _{1$\bar{1}$0} (46.7)	30.9 _{11$\bar{2}$} (46.7)

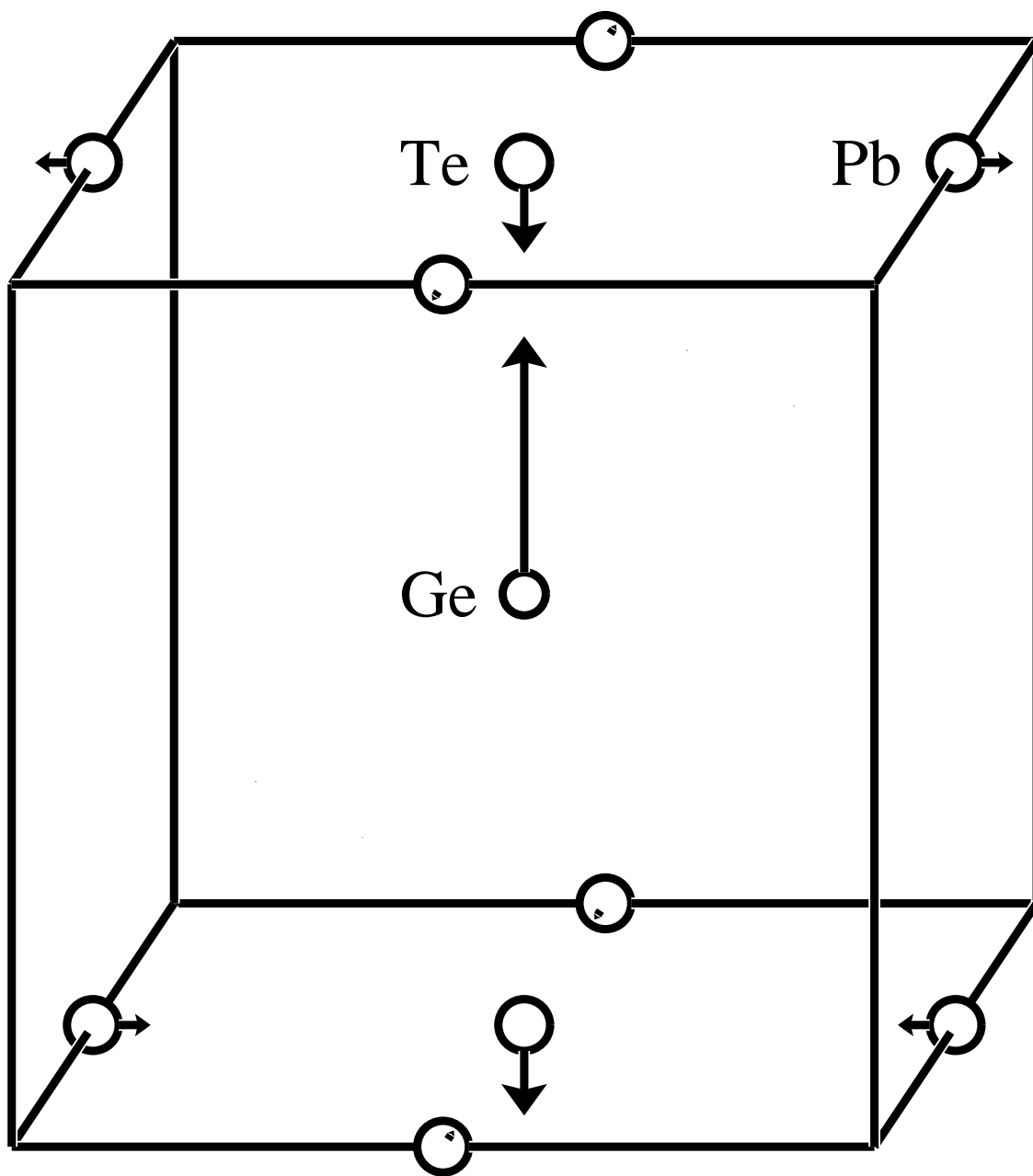


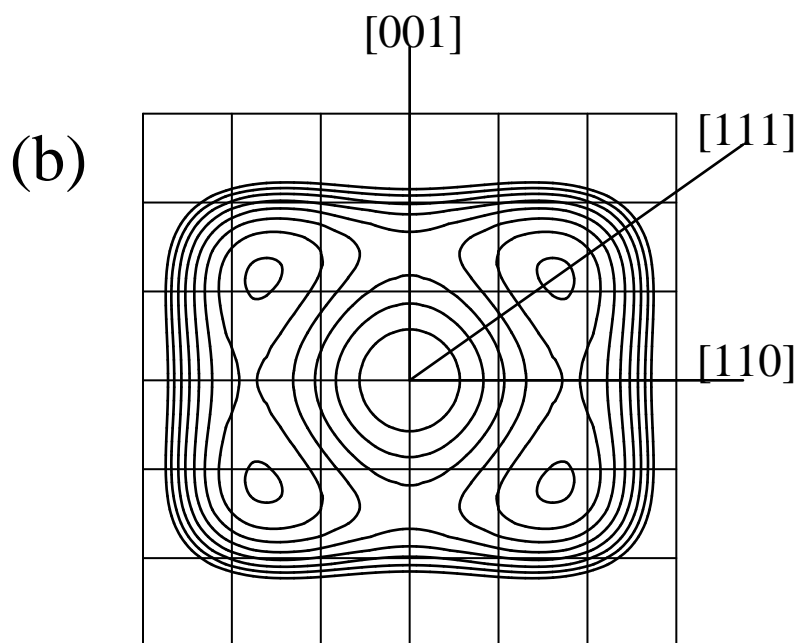
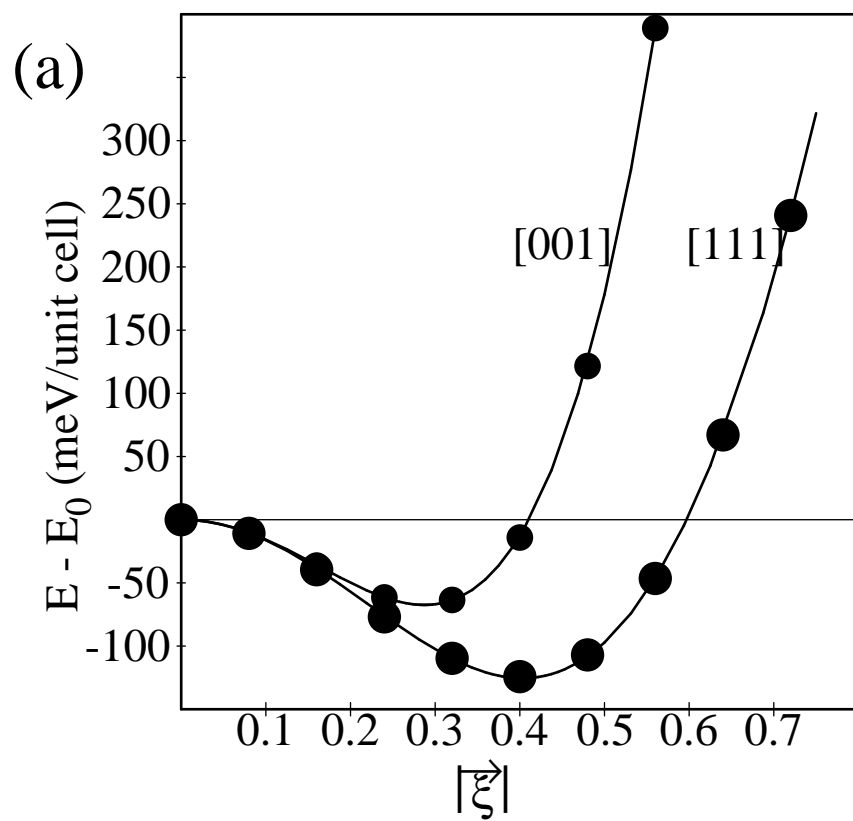


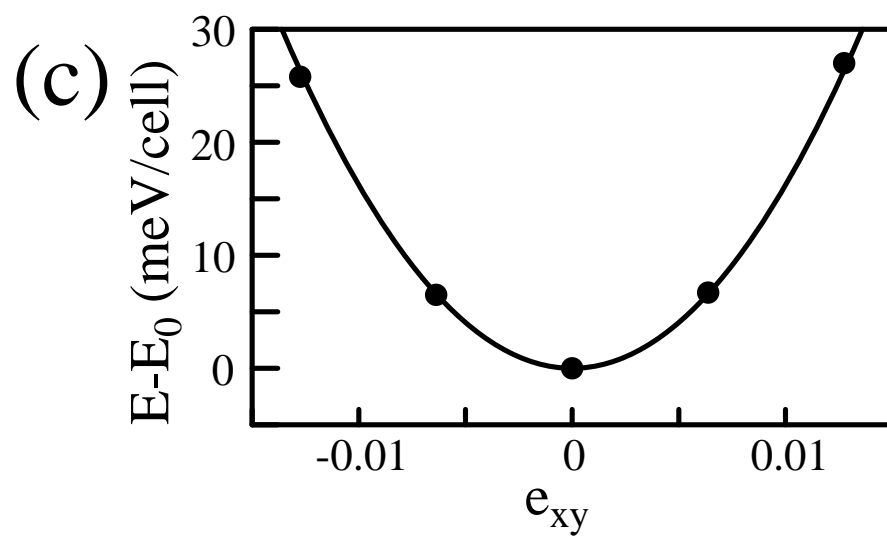
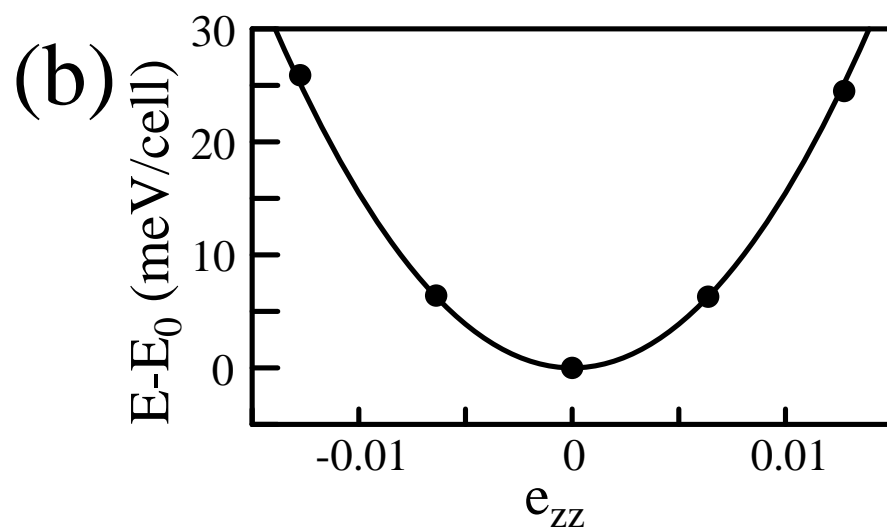
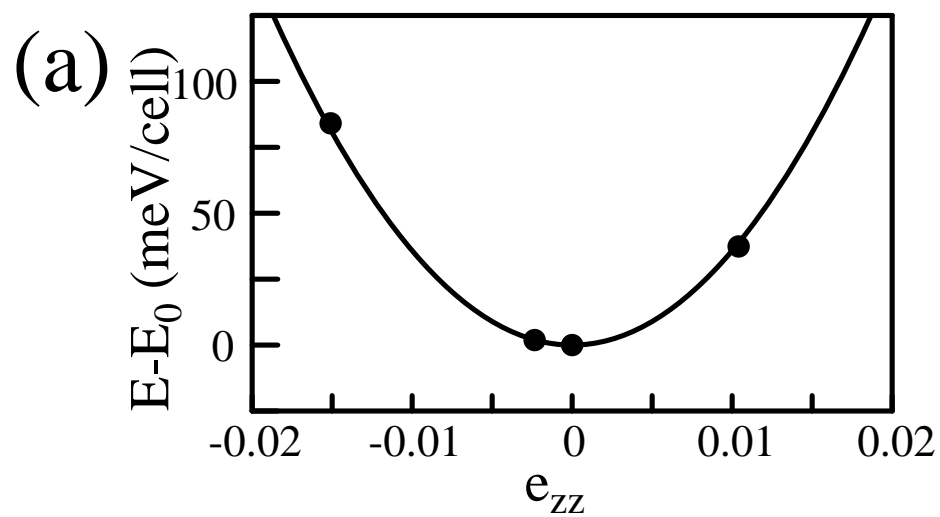
 Pb

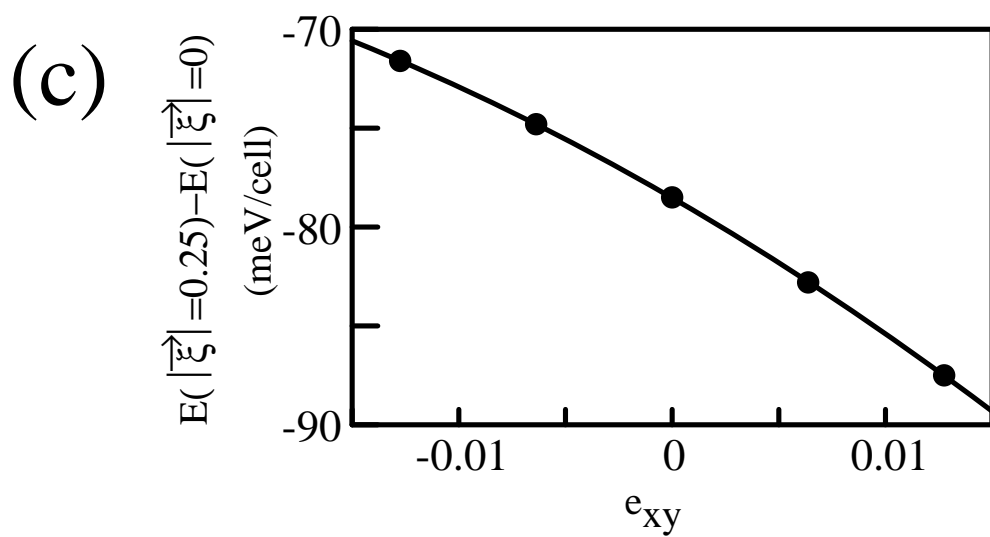
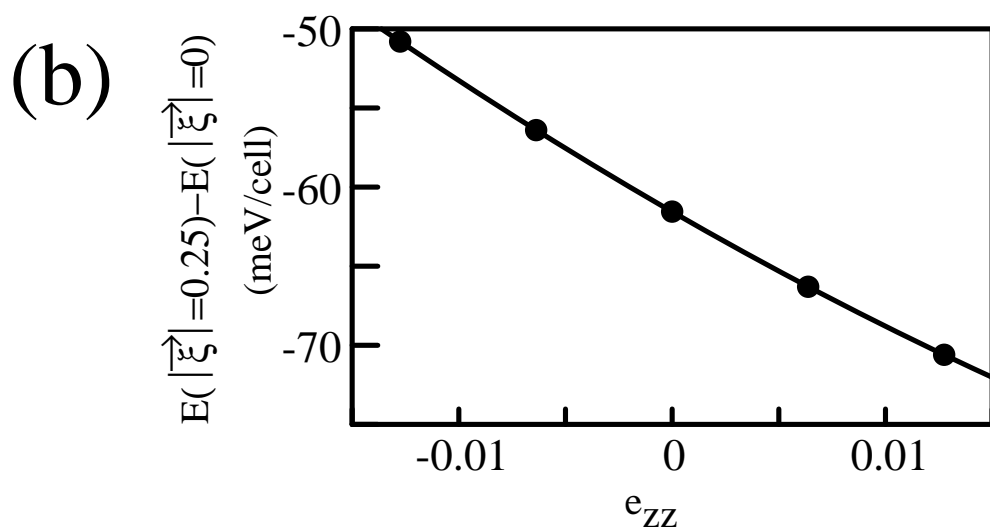
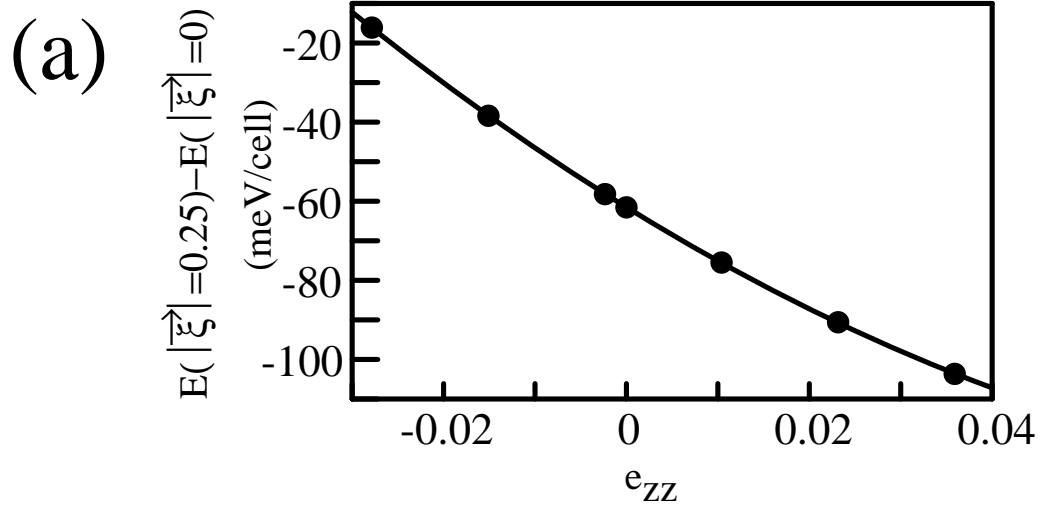
 Ge

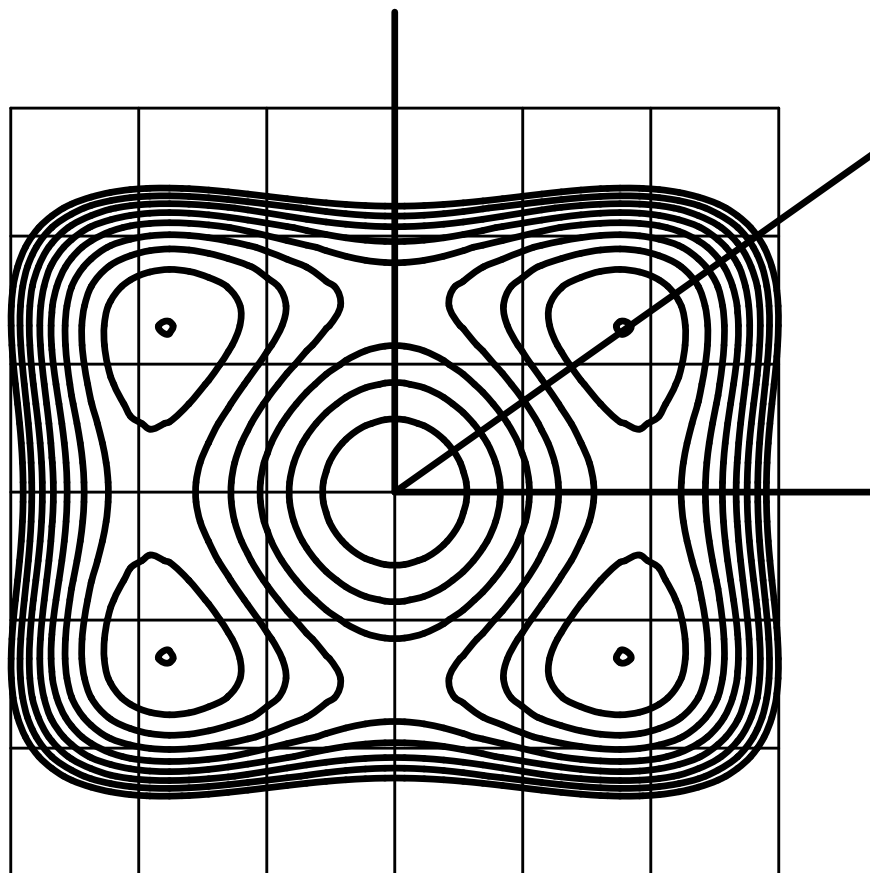
 Te



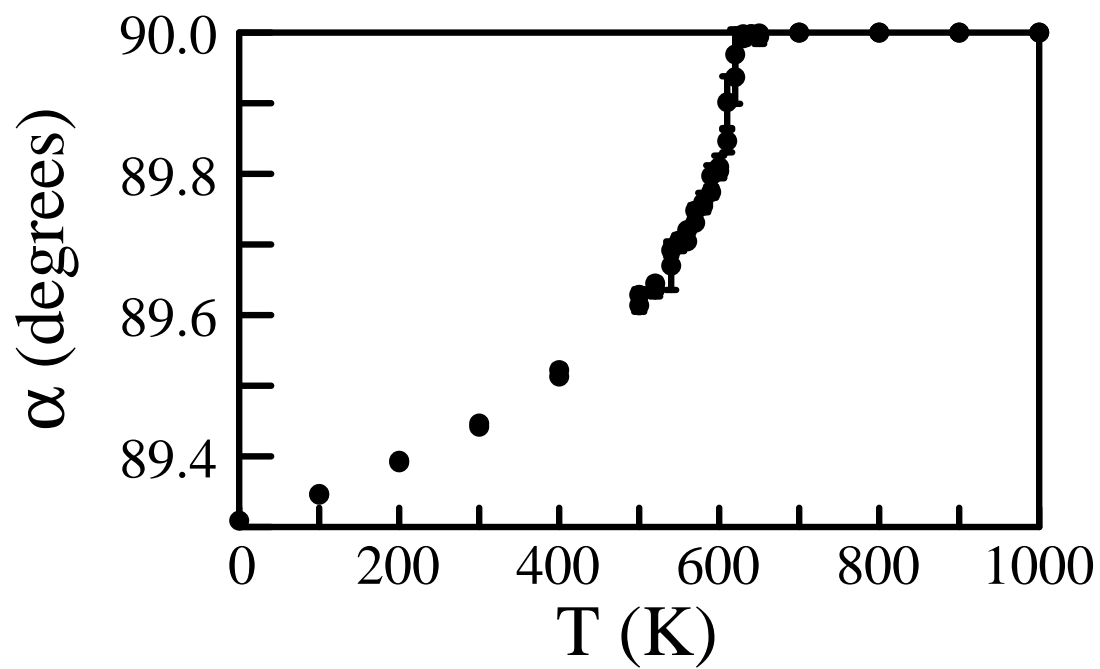








(a)



(b)

